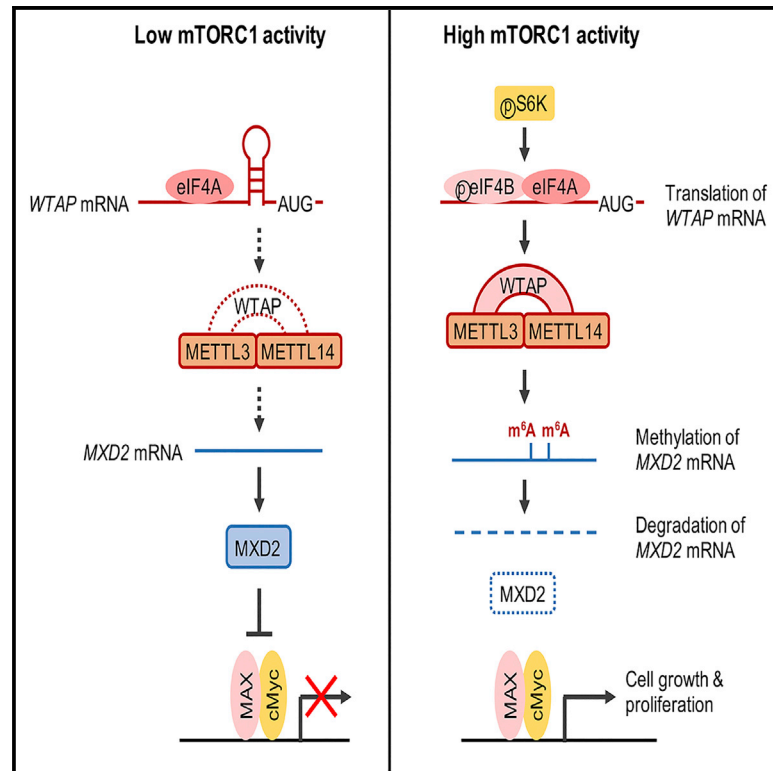# mTORC1 promotes cell growth via m^{6}A-dependent mRNA degradation

Graphical abstract

Authors

Sungyun Cho, Gina Lee,
Brian F. Pickering, ...,
Norbert Perrimon, Samie R. Jaffrey,
John Blenis

Correspondence

ginalee@uci.edu (G.L.),
srj2003@med.cornell.edu (S.R.J.),
job2064@med.cornell.edu (J.B.)

In brief

Cho et al. report that mTORC1 enhances WTAP translation through eIF4A/4B, resulting in the increase of global mRNA m^{6}A modification. m^{6}A modification of mRNAs by mTORC1 destabilizes transcripts through YTHDF m^{6}A-reader proteins. Among the targets, mTORC1 increases m^{6}A modification on MXD2 mRNA, cMyc suppressor, resulting in increased cMyc activity and tumor growth.

Highlights

- mTORC1 induces WTAP translation through eIF4A/4B

- mTORC1-WTAP increases global m^{6}A levels on mRNA

- Increased m^{6}A modification by mTORC1 destabilizes mRNAs

- mTORC1 decreases mRNA expression of MXD2, cMyc suppressor, through m^{6}A modification

CellPress

Molecular Cell

CellPress

Article

mTORC1 promotes cell growth via m^{6}A-dependent mRNA degradation

Sungyun Cho,[1,10] Gina Lee,[1,2,10,*] Brian F. Pickering,[1,10] Cholsoon Jang,[3,4] Jin H. Park,[1] Long He,[1] Lavina Mathur,[2] Seung-Soo Kim,[5] Sunhee Jung,[4] Hong-Wen Tang,[6,7] Sebastien Monette,[8] Joshua D. Rabinowitz,[3] Norbert Perrimon,[6,9] Samie R. Jaffrey,[1,*] and John Blenis[1,11,*]

[1]Department of Pharmacology, Meyer Cancer Center, Weill Cornell Medicine, Cornell University, New York, NY, USA
[2]Department of Microbiology and Molecular Genetics, Chao Family Comprehensive Cancer Center, University of California Irvine School of Medicine, Irvine, CA, USA
[3]Department of Chemistry, Lewis Sigler Institute for Integrative Genomics, Princeton University, Princeton, NJ, USA
[4]Department of Biological Chemistry, Chao Family Comprehensive Cancer Center, University of California Irvine School of Medicine, Irvine, CA, USA
[5]Department of Obstetrics and Gynecology, Irving Medical Center, Columbia University, New York, NY, USA
[6]Department of Genetics, Blavatnik Institute, Harvard Medical School, Boston, MA, USA
[7]Program in Cancer and Stem Cell Biology, Duke-NUS Medical School, Singapore, Singapore
[8]Laboratory of Comparative Pathology, Memorial Sloan Kettering Cancer Center, The Rockefeller University, Weill Cornell Medicine, New York, NY, USA
[9]Howard Hughes Medical Institute, Boston, MA, USA
[10]These authors contributed equally
[11]Lead contact
*Correspondence: ginalee@uci.edu (G.L.), srj2003@med.cornell.edu (S.R.J.), job2064@med.cornell.edu (J.B.)
https://doi.org/10.1016/j.molcel.2021.03.010

SUMMARY

Dysregulated mTORC1 signaling alters a wide range of cellular processes, contributing to metabolic disorders and cancer. Defining the molecular details of downstream effectors is thus critical for uncovering selective therapeutic targets. We report that mTORC1 and its downstream kinase S6K enhance eIF4A/4B-mediated translation of *Wilms' tumor 1-associated protein* (WTAP), an adaptor for the N^6-methyladenosine (m^{6}A) RNA methyltransferase complex. This regulation is mediated by 5′ UTR of *WTAP* mRNA that is targeted by eIF4A/4B. Single-nucleotide-resolution m^{6}A mapping revealed that *MAX dimerization protein 2* (*MXD2*) mRNA contains m^{6}A, and increased m^{6}A modification enhances its degradation. WTAP induces cMyc-MAX association by suppressing MXD2 expression, which promotes cMyc transcriptional activity and proliferation of mTORC1-activated cancer cells. These results elucidate a mechanism whereby mTORC1 stimulates oncogenic signaling via m^{6}A RNA modification and illuminates the WTAP-MXD2-cMyc axis as a potential therapeutic target for mTORC1-driven cancers.

INTRODUCTION

The mechanistic target of rapamycin complex 1 (mTORC1) is an evolutionarily conserved serine/threonine kinase that senses environmental cues and regulates a diverse array of physiological processes (Saxton and Sabatini, 2017; Shimobayashi and Hall, 2014). Once activated, mTORC1 promotes synthesis of macromolecules including nucleotides, proteins, and lipids while inhibiting catabolic processes such as autophagy (Gomes and Blenis, 2015; Jewell and Guan, 2013). Activation of mTORC1 signaling has been reported in ~80% of human cancers including the genetic tumor syndromes, tuberous sclerosis complex (TSC), and lymphangioleiomyomatosis (LAM) (Lam et al., 2018; Mossmann et al., 2018).

mTORC1 also regulates diverse aspects of mRNA metabolism. For example, mTORC1 promotes mRNA translation

through its downstream proteins, ribosomal protein S6 kinase (S6K) and eukaryotic initiation factor 4E (eIF4E)-binding protein (4E-BP) (Hinnebusch et al., 2016; Kimball and Jefferson, 2006; Ma and Blenis, 2009). mTORC1-activated S6K promotes recruitment of eIF4B into the translation pre-initiation complex where the eIF4A/4B RNA helicase unwinds highly structured 5′ untranslated regions (5′ UTRs) in specific mRNAs to enhance their translation efficiency (Csibi et al., 2014; Holz et al., 2005; West et al., 1998). mTORC1 also promotes splicing and polyadenylation of a subset of genes to increase mRNA stability and translation (Chang et al., 2015; Lee et al., 2017; Ma et al., 2008; Tang et al., 2018a). Thus, mTORC1 plays crucial roles in supporting cell growth and proliferation through regulation of RNA metabolic processes at global and gene-specific levels.

RNA processing and quality control are pivotal nodes of gene expression control during cell fate decisions and disease

development (Gilbert et al., 2016; Gott and Emeson, 2000). One of the most well-studied RNA chemical modifications is the N^6-adenosine methylation (m^{6}A) of mRNA (Fu et al., 2014; Meyer and Jaffrey, 2017). m^{6}A is generated by nuclear methyltransferases, termed "writers," which includes the heterodimeric methyltransferase METTL3-METTL14, and the adaptor protein WTAP, which is required for m^{6}A formation and localization of METTL3-METTL14 to the nucleus (Ping et al., 2014; Schwartz et al., 2014). Subsequently, the m^{6}A-reader proteins such as the YTH domain-containing protein family bind to the m^{6}A-containing mRNAs to control their fates, including splicing, intracellular localization, and stability (Patil et al., 2018). Alterations in m^{6}A modifications on transcripts encoding oncogenes and tumor suppressors induce malignancies in leukemia, glioma, and breast and lung cancers (Barbieri and Kouzarides, 2020; Huang et al., 2020). However, very little is known about how the m^{6}A modification process is controlled by cellular signal transduction pathways in these conditions.

Here, we uncover an important role for the mTORC1 pathway in stimulating global and gene-specific mRNA methylation. We show that mTORC1-activated eIF4A/4B enhances the translation of *WTAP* mRNA, which encodes a central component of the m^{6}A methyltransferase writer complex. Additionally, through single-nucleotide-resolution transcriptome-wide m^{6}A mapping, we discover the MXD2-cMyc axis as an important downstream effector of mTORC1-mediated m^{6}A RNA modification in promoting cell growth and proliferation. Our findings provide a rationale for the development of therapeutics targeting RNA modification events to treat mTORC1-driven diseases.

RESULTS

mTOR stimulates global m^{6}A levels

Given that mTOR regulates multiple steps of mRNA quality control (Chang et al., 2015; Lee et al., 2017; Ma et al., 2008; Tang et al., 2018a), we speculated that mTOR may also regulate mRNA chemical modifications. We measured m^{6}A levels in poly(A)-RNA isolated from insulin-treated HEK293E cells using liquid chromatography mass spectrometry (LC-MS) (Jia et al., 2011). Insulin did not significantly change global m^{6}A levels until 12 h, after which they continued to increase by ~30%–50% after 30 h insulin treatment (Figure 1A; Figure S1A). Conversely, inhibition of mTOR activity with catalytic inhibitor torin1 suppressed insulin-induced m^{6}A modification (Figures 1B–1D). Thus, mTOR activation promotes m^{6}A modification of mRNAs.

We next sought to investigate mTOR-dependent changes in individual m^{6}A sites on transcripts. To this end, we performed transcriptome-wide m^{6}A mapping using m^{6}A individual-nucleotide-resolution cross-linking and immunoprecipitation (miCLIP) (Linder et al., 2015). Consistent with the globally decreased m^{6}A levels, torin1 decreased the abundance of read counts on individual m^{6}A sites (Figure 1E). The m^{6}A writer complex preferentially deposits m^{6}A on the consensus sequence, DRA*CH (D = G/A/U, R = G/A, A* = m^{6}A, H = U/A/C), and the m^{6}A modification is generally enriched around the last exon (Dominissini et al., 2012; Meyer et al., 2012). Interestingly, torin1 did not specifically alter the m^{6}A consensus motif (Figure 1F) nor the distribution of

m^{6}A across the transcript body (Figure 1G), indicating that mTOR signaling affects the global activity of the m^{6}A methyltransferase.

mTORC1-S6K pathway induces WTAP expression

To elucidate molecular mechanisms of how mTOR regulates m^{6}A methyltransferase activity, we examined protein levels of the core m^{6}A methyltransferase complex, METTL3, METTL14, and WTAP. Upon insulin stimulation, the protein level of WTAP was markedly induced, whereas the levels of METTL3 and METTL14 were not affected (Figure 1H). Consistent with m^{6}A induction by 30 h insulin treatment (Figure S1A), WTAP expression was gradually increased by insulin and was highest at 30 h (Figure S1B). Inhibition of mTOR activity by torin1 treatment or *mTOR* silencing by siRNA suppressed WTAP expression (Figures 1I and 1J). Knockdown of *WTAP* suppressed insulin-induced m^{6}A levels (Figures 1K and 1L), indicating that WTAP is required for the mTOR-dependent m^{6}A modification.

mTOR forms two distinct complexes, mTOR complex 1 and 2 (mTORC1 and mTORC2), with their respective key components Raptor and Rictor (Kim et al., 2002; Sarbassov et al., 2005). To investigate which mTOR complex regulates WTAP, we silenced *Raptor* or *Rictor*. As a result, *Raptor* knockdown, but not *Rictor* knockdown, significantly reduced WTAP levels (Figure 2A), indicating that mTORC1 regulates WTAP expression. Treatment of the mTORC1-specific inhibitor rapamycin suppressed insulin-induced WTAP expression (Figure 2B). In cancer cell panels with overactive mTORC1 signaling, WTAP expression was suppressed by rapamycin and torin1 treatment (Figures 2C–2F). In patient-derived *TSC2*-deficient LAM cell line (Yu et al., 2004), reconstitution of *TSC2* markedly reduced WTAP protein levels (Figure 2G). Thus, mTORC1 activity is required for WTAP protein expression.

To further examine the regulation of WTAP by mTORC1 *in vivo*, we used a *Tsc2*-heterozygote mouse model (*Tsc2*$^{+/-}$), which spontaneously develops kidney tumors via loss of heterozygosity (Onda et al., 1999; Woodrum et al., 2010). In the kidneys of these mice, mTORC1 was active as measured by increased phosphorylation of ribosomal protein S6 (pS6) compared to the normal kidneys (Figure 2H). WTAP expression was also markedly induced (Figure 2H). Administration of rapamycin to these mice suppressed both pS6 and WTAP levels (Figure 2H). Rapamycin also reduced tumor burden, measured by the decreased number and area of the tumors detected by magnetic resonance imaging (MRI) and hematoxylin and eosin (H&E) staining (Figures 2I and 2J) (Kalogerou et al., 2012; Lee et al., 2009).

S6K1/2 is a key downstream effector of mTORC1 (Holz and Blenis, 2005; Schalm et al., 2005). Indeed, knockdown of *S6K1/2* reduced WTAP expression (Figure 2K). Expression of a constitutively active form of S6K1 (S6K1-CA) (Schalm et al., 2005) restored WTAP expression upon rapamycin treatment (Figure 2L). Therefore, the mTORC1-S6K axis regulates WTAP expression.

eIF4A/4B induces WTAP protein translation

We next investigated the mechanism of how mTORC1-S6K signaling regulates WTAP expression. Unexpectedly, expression levels of *WTAP* mRNA did not correlate with protein
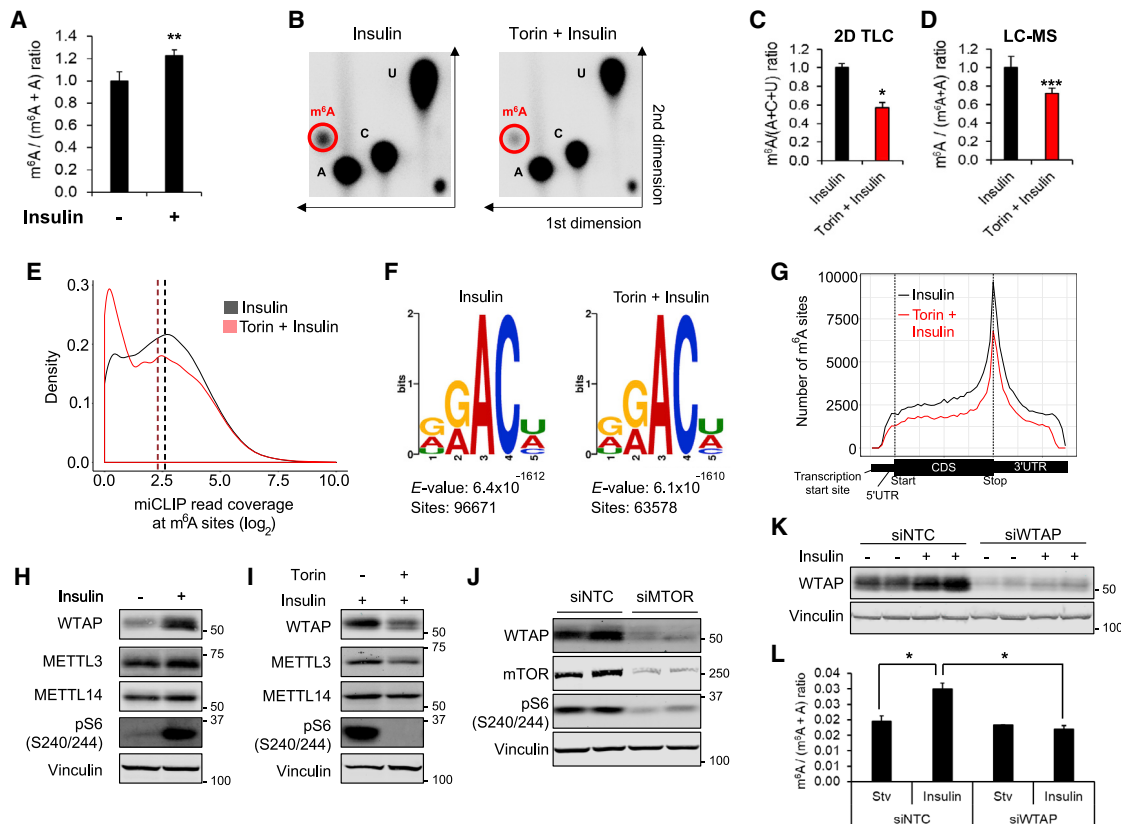
Figure 1. mTOR induces m^{6}A modification of mRNAs

(A) LC-MS analysis of m^{6}A levels in twice-purified poly(A)-RNA from HEK293E cells. Cells were treated with insulin (200 nM, 30 h) after overnight serum starvation.

(B and C) Two-dimensional thin-layer chromatograph (2D TLC, B) analysis of nucleotide levels in HEK293E cells. Cells were serum starved overnight and treated with insulin (200 nM, 30 h) with or without pretreatment of torin1 (250 nM). Twice-purified poly(A)-RNAs were digested with nuclease T1 and radio-labeled with ^{32}P-ATP. (C) shows quantification of the intensity of nucleotide spots in (B).

(D) LC-MS analysis of m^{6}A levels in HEK293E cells serum starved overnight and treated with insulin (200 nM, 30 h) with or without pretreatment of torin1 (250 nM).

(E) Density plot of m^{6}A read coverage at m^{6}A sites. miCLIP was performed in HEK293E cells serum starved overnight and treated with insulin (200 nM, 30 h) with or without pretreatment of torin1 (250 nM). The log$_2$ value of miCLIP reads was calculated at each m^{6}A site. A density plot represents changes at miCLIP reads at individual sites. The mean read density for each sample is indicated by dashed vertical lines.

(F) MEME-ChIP motif enrichment analysis of miCLIP reads.

(G) Metagene plot of the frequency of m^{6}A sites throughout the transcript body.

(H) Immunoblot analysis of HEK293E cells treated with insulin (200 nM, 30 h) after overnight serum starvation.

(I) Immunoblot analysis of HEK293E cells serum starved overnight and treated with insulin (200 nM, 30 h) with or without pretreatment of torin1 (250 nM).

(J) Immunoblot analysis of HEK293E cells treated with siRNA against non-targeting control (NTC) or *mTOR*.

(K and L) Immunoblot (K) and LC-MS (L) analysis of HEK293E cells stimulated with insulin (200 nM, 30 h) after overnight serum starvation. Cell were treated with siRNA against non-targeting control (NTC) or *WTAP*.

n = 3. *p < 0.05, **p < 0.01, ***p < 0.001. Error bars show standard deviation (SD).

expression (Figures 3A and 3B). This suggests that mTORC1-S6K signaling increases WTAP protein expression via post-transcriptional mechanisms. We and others have shown that mTORC1-S6K promotes translation of mRNAs with a highly structured 5′ UTR via recruitment of eIF4A/4B into the translation preinitiation complex. eIF4A unwinds highly structured 5′ UTR with its RNA helicase activity, thereby increasing the efficiency of target mRNA translation (Csibi et al., 2014; Holz et al., 2005; Shahbazian et al., 2010).

Intriguingly, computational structure-prediction analysis based on the primary RNA sequence (Lorenz et al., 2011) indicated that the 5′ UTR of *WTAP* is highly structured, with very

low Gibbs free energy (ΔG = −158.50 kcal/mol) (Figure 3C). This complexity is comparable to that of well-known eIF4A/4B target genes such as *cMyc*, *ODC1*, and *BCL2* (Figure 3C) (Csibi et al., 2014; Shahbazian et al., 2010). In contrast, *METTL3* or *METTL14* 5′ UTRs contain much simpler secondary structures (Figure 3C). Knockdown of *eIF4A1/2* or *eIF4B* significantly reduced WTAP protein levels as well as global m^{6}A levels (Figures 3D and 3E; Figures S2A and S2B).

We then measured translation efficiency of *WTAP* mRNA using a polysome profiling assay (Figures S2C and S2D). Knockdown of *eIF4A* shifted *WTAP* mRNA toward lighter polysomal fractions (Figure 3F), indicating that *WTAP* translation is suppressed. In
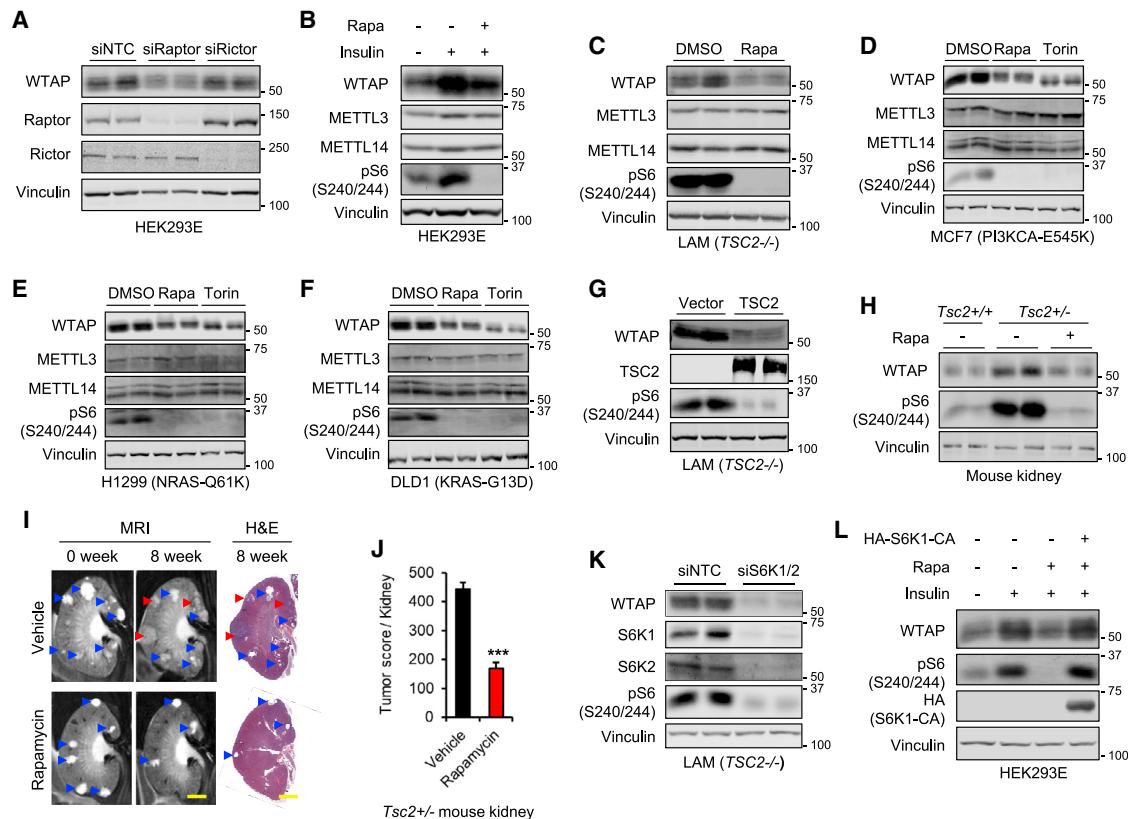
Figure 2. mTORC1-S6K1 signaling regulates WTAP expression

(A) Immunoblot analysis of HEK293E cells treated with siRNAs against each denoted gene.

(B) Immunoblot analysis of HEK293E cells serum starved overnight and treated with insulin (200 nM, 30 h) with or without pretreatment of rapamycin (100 nM).

(C–F) Immunoblot analysis of human LAM 621-101 (C), MCF7 (D), H1299 (E), and DLD1 (F) cells treated with rapamycin (100 nM, 24 h) or torin1 (250 nM, 24 h).

(G) Immunoblot analysis of LAM 621-101 ($TSC2^{-/-}$) cells expressing empty vector or $TSC2$.

(H) Immunoblot analysis of kidney from wild-type ($Tsc2^{+/+}$) and $Tsc2$ heterozygous ($Tsc2^{+/-}$) mice treated with vehicle or rapamycin (8 mg/kg) for 8 weeks.

(I) Representative magnetic resonance imaging (MRI) and histology (H&E-stained sections) images of kidneys from $Tsc2^{+/-}$ mice before and after vehicle or rapamycin (8 mg/kg) treatment for 8 weeks. Blue arrowheads indicate cysts and papillary lesions. Red arrowheads indicate solid tumors. Scale bars, 2 mm.

(J) Tumor score was calculated by the sum of the tumor lesion area from H&E images. $Tsc2^{+/-}$ mice were treated with vehicle or rapamycin (8 mg/kg) for 8 weeks. n = 6. ***p < 0.001. Error bars show standard error of the mean (SEM).

(K) Immunoblot analysis of LAM 621-101 ($TSC2^{-/-}$) cells treated with siRNAs against each denoted gene.

(L) Immunoblot analysis of HEK293E cells transfected with empty vector or constitutively active S6K1-CA (S6K1-F5A/R3A/T389E). Cells were serum starved overnight and treated with insulin (200 nM, 30 h) with or without pretreatment of rapamycin (100 nM).

contrast, the mRNA distribution of a control gene, *PPIB*, which contains an unstructured 5′ UTR (Figure 3C), was not shifted (Figure 3G). Furthermore, a small-molecule inhibitor of eIF4A, silvestrol (Bordeleau et al., 2008), decreased WTAP protein levels (Figure 3H). This effect was markedly abrogated in the WTAP construct that lacks its 5′ UTR (Figure 3I; Figure S2E). Collectively, these results demonstrate that mTORC1-S6K induces WTAP protein expression via eIF4A-mediated mRNA translation.

mTORC1 decreases mRNA levels via m6A modification

To explore the biological impact of mTORC1-mediated m6A modification, we revisited our m6A sequencing data that compared transcriptome-wide m6A levels between DMSO- and torin1-treated cells (Figures 1E–1G). While mRNA levels were globally decreased by mTORC1 inhibition, consistent with mTORC1's role in promoting nucleotide synthesis (Ben-

Sahra et al., 2016; Düvel et al., 2010; Valvezan et al., 2017), to our surprise, the mRNAs whose expression increased after torin1 treatment were enriched in annotated m6A sites (Figure 4A). This is in line with the previous studies showing that m6A destabilizes mRNAs and inhibition of m6A deposition on these transcripts leads to increased mRNA stability (Sommer et al., 1978). This raises the possibility that the biological roles of mTORC1 in promoting cell growth and proliferation may be mediated, in part, by enhancing WTAP levels, which leads to increased m6A formation and subsequent degradation of specific transcripts.

Therefore, we followed up on those genes whose m6A levels are decreased while mRNA levels are increased by torin1 (Figure S3). Normalization of m6A levels on each gene by transcript abundance gave 2,439 genes whose m6A levels are significantly decreased by torin1 (Tables S1A and S1B). Among these, we
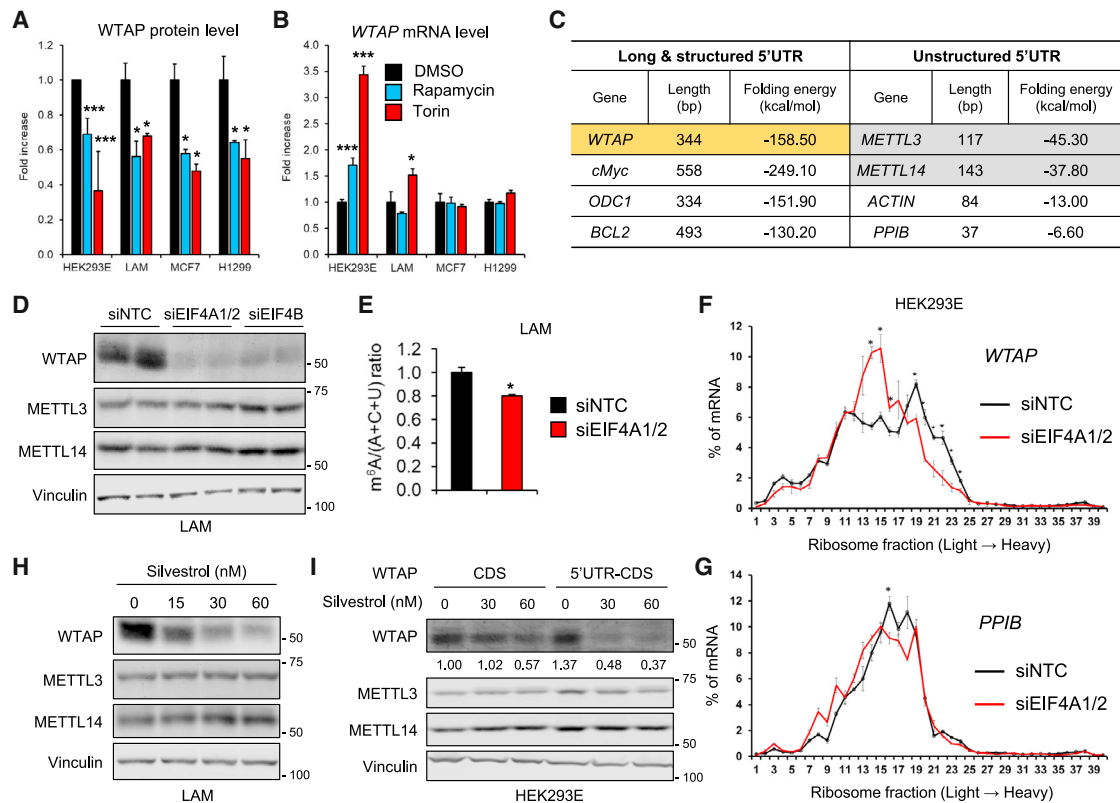
Figure 3. eIF4A/4B promotes translation of *WTAP*
(A and B) Quantification of immunoblot results (A) or qPCR analysis (B) of WTAP in HEK293E, LAM, MCF7, and H1299 cells with or without rapamycin (100 nM) or torin1 (250 nM). n = 3. *p < 0.05, ***p < 0.001. Error bars show SD.
(C) Analysis of the nucleotide length and Gibbs free energy of 5′ UTR.
(D) Immunoblot analysis of LAM 621-101 (*TSC2*−/−) cells treated with siRNAs against each denoted gene.
(E) Quantification of the 2D TLC analysis of nucleotide levels in LAM 621-101 (*TSC2*−/−) cells. Cells were treated with siRNAs against each denoted gene. n = 2. *p < 0.05. Error bars show SD.
(F and G) qPCR analysis of sucrose-gradient polysome fractions of HEK293E cells treated with siRNAs against each denoted gene. n = 2. *p < 0.05. Error bars show SEM.
(H) Immunoblot analysis of LAM 621-101 (*TSC2*−/−) cells treated with silvestrol for 24 h.
(I) Immunoblot analysis of *WTAP* knockout HEK293E cells transfected with empty vector or *WTAP* containing coding region (CDS) or 5′ UTR and CDS (5′ UTR-CDS). Cells were treated with silvestrol for 24 h. Numbers below each band show the quantification of band intensity normalized by loading control.

probed for the genes whose mRNA levels are significantly increased by torin1. Statistical analysis of this set of genes narrowed down our list of most significant candidates to 199 genes (Table S1C). Gene Ontology (GO) analysis (Huang et al., 2009) revealed that over half of the genes were enriched in cellular macromolecule metabolic processes (Table S1D). Other cellular functions such as protein *O*-linked mannosylation, protein targeting, and gene silencing were also enriched (Table S1D). We then focused on 105 genes associated with cellular macromolecule metabolic processes and performed qPCR to confirm the changes in mRNA levels. For the qPCR analysis, we tested the following conditions in *TSC2*-deficient LAM cells: (1) to verify mTORC1 dependency, we treated with torin1, and (2) to verify m6A dependency, we knocked down *METTL3/METTL14* or *WTAP* (Tables S2A and S2B; Figures S4A and S4B). As a result of our analysis, the mRNA levels of 18 genes, including *MAX dimerization protein 2* (*MXD2,* also known as

Max interactor 1 or *MXI1*), *Fibroblast growth factor receptor 1* (*FGFR1*), and *FGFR3*, were consistently and statistically significantly increased in all three conditions (Figures 4B–4D; Figure S3; Table S2C).

mTORC1 suppresses *MAX dimerization protein 2* (*MXD2*) expression by m6A modification

Among the m6A sequencing candidate genes (Table S2C), it was of particular interest that mTORC1 can potentially regulate cMyc signaling via m6A modification of cMyc suppressor *MXD2*. MXD proteins are known to inhibit cMyc activity by competing with cMyc transcriptional co-activator Max (Mathsyaraja et al., 2019; Schreiber-Agus et al., 1995, 1998). Among the MXD family proteins, only the expression of *MXD2*, not *MXD1*, *MXD3*, or *MXD4*, was increased by rapamycin (Figure S4C). Rapamycin and torin1 significantly induced *MXD2* mRNA levels in multiple cancer cell lines with overactive mTORC1 signaling (Figure 4E),
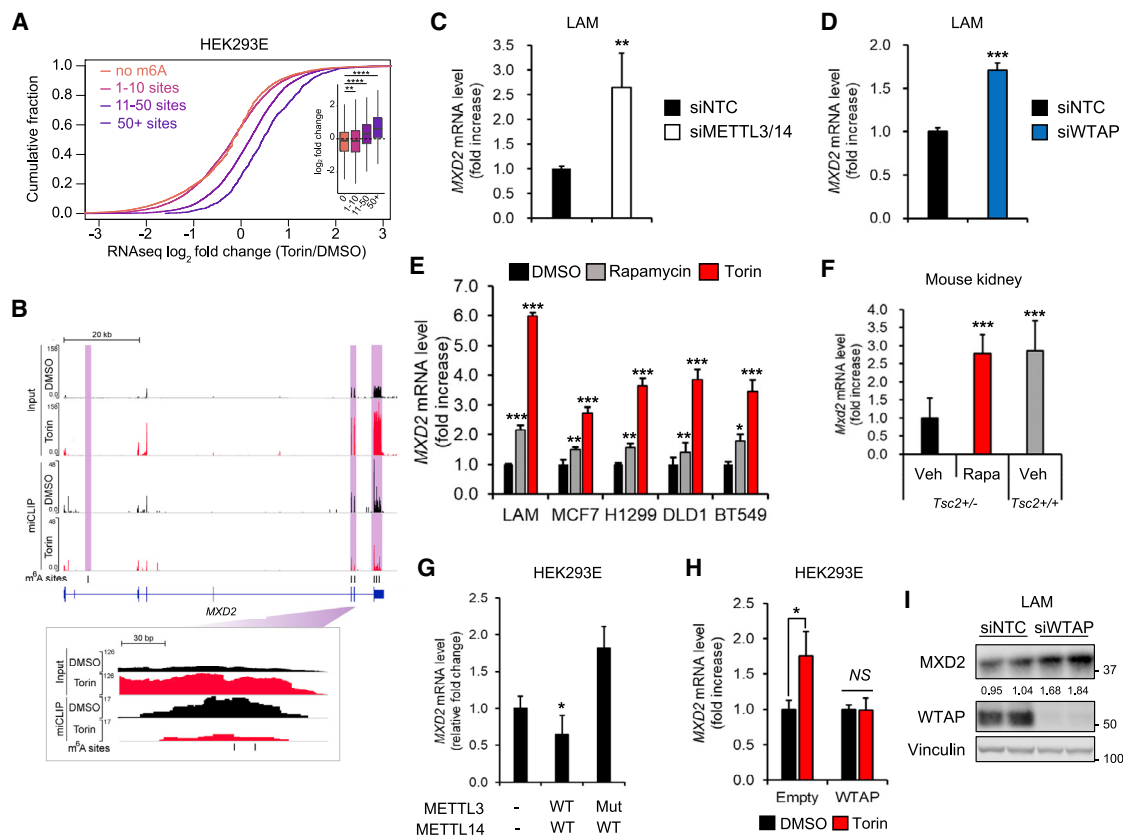
Figure 4. mTORC1 and m⁶A enzymes suppress *MXD2* expression

(A) Cumulative distribution plot of transcript abundance from RNA-seq of miCLIP input samples in Figure 1 (DMSO versus torin1). Transcripts were binned based on number of called m⁶A sites in DMSO samples. The log_2 fold change in torin1 over DMSO was calculated for each transcript. Inset is a boxplot of the same data. Statistical significance was determined using Tukey's HSD test.

(B) Genome tracks of miCLIP and input RNA-seq coverage on *MXD2*. Areas containing m⁶A sites (black dashes) are highlighted with purple boxes.

(C) qPCR analysis of *MXD2* in LAM 621-101 ($TSC2^{-/-}$) cells knocked down with *METTL3* and *METTL14*.

(D) qPCR analysis of *MXD2* in LAM 621-101 ($TSC2^{-/-}$) cells knocked down with *WTAP*.

(E) qPCR analysis of *MXD2* in LAM 621-101 ($TSC2^{-/-}$), MCF7, H1299, DLD1, and BT549 cells treated with rapamycin (100 nM, 24 h) or torin1 (250 nM, 24 h).

(F) qPCR analysis of *Mxd2* in $Tsc2^{+/+}$ and $Tsc2^{+/-}$ mouse kidneys treated with vehicle or rapamycin (8 mg/kg) for 8 weeks.

(G) qPCR analysis of *MXD2* in HEK293E cells expressing METTL14 with METTL3-WT or METTL3-Mut (amino acids 395–398 converted from DPPW to APPA). Cells were serum starved overnight and treated with insulin (200 nM, 30 h). Relative fold change was calculated by normalizing *MXD2* mRNA levels in siMETTL3/14 compared to siNTC in each condition.

(H) qPCR analysis of *MXD2* in HEK293E cells expressing WTAP. The cells were serum starved overnight and treated with insulin (200 nM, 30 h) with or without pretreatment of torin1 (250 nM).

(I) Immunoblot analysis of *MXD2* in LAM 621-101 ($TSC2^{-/-}$) cells treated with siRNAs against each denoted gene.

n = 3. *$p < 0.05$, **$p < 0.01$, ***$p < 0.001$, ****$p < 0.0001$. Error bars show SD.

suggesting that mTORC1 suppresses *MXD2* expression in various cancers. In *Tsc2*-deficient mouse kidney tumors, *Mxd2* mRNA level was markedly decreased compared to control, which was restored by rapamycin treatment (Figure 4F). In HEK293E cells depleted of endogenous METTL3-METTL14, expression of wild-type METTL3 with METTL14, but not the catalytic inactive mutant (METTL3-D395A/W398A) (Lin et al., 2016; Wang et al., 2016), suppressed *MXD2* levels (Figure 4G; Figure S4D). Furthermore, a METTL3 catalytic inactive mutant increased *MXD2* expression, consistent with a dominant-negative effect of this mutation. Ectopic expression of *WTAP* suppressed torin1-induced *MXD2* expression (Figure 4H; Figure S4E). Finally, MXD2 protein levels were induced by *WTAP*

knockdown (Figure 4I) and decreased by insulin treatment (Figure S4F).

Once mRNAs are modified with m⁶A, the m⁶A-binding proteins are recruited to determine the fate of mRNAs (Patil et al., 2018). Among these m⁶A readers, YTHDF proteins degrade m⁶A-modified mRNAs (Lasman et al., 2020; Wang et al., 2014; Zaccara and Jaffrey, 2020). Indeed, knockdown of *YTHDF2/3* increased expression of *MXD2* (Figure 5A; Figure S4G), indicating that mTORC1-dependent m⁶A modification decreases *MXD2* mRNA stability. Assessment of *MXD2* mRNA levels upon transcription inhibition or by 5-ethynyl uridine (5-EU) labeling revealed that rapamycin and torin1 increase the stability of *MXD2* mRNA (Figures 5B–5D).
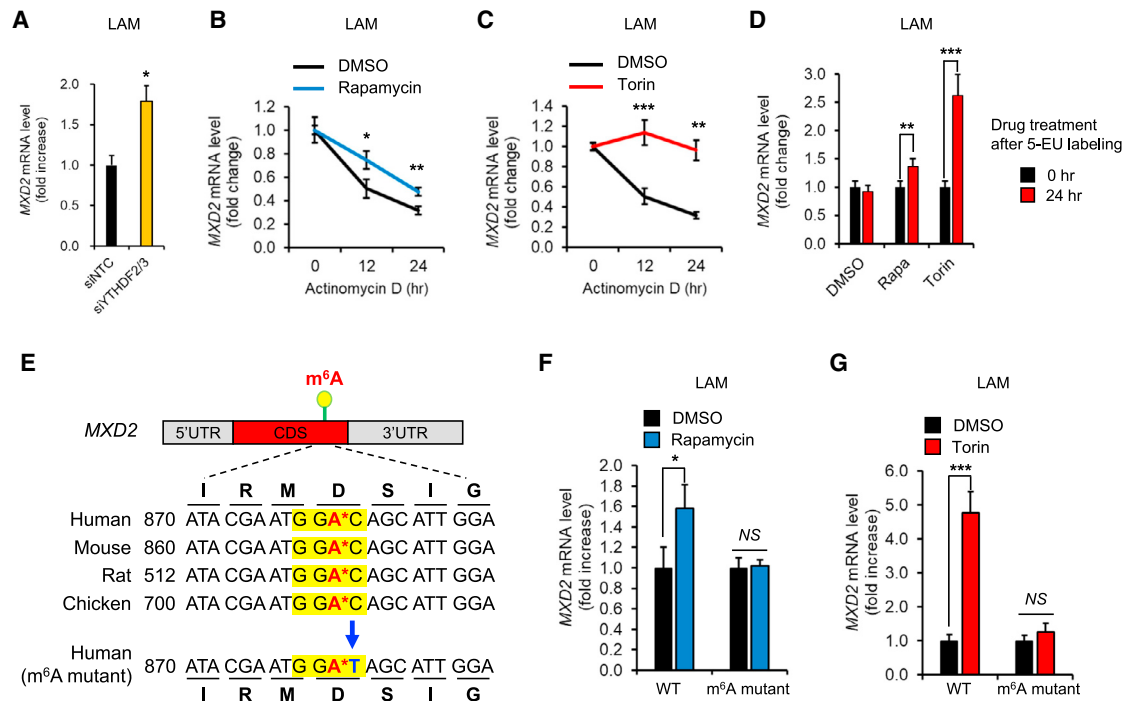
Figure 5. mTORC1 decreases *MXD2* mRNA stability via m6A modification

(A) qPCR analysis of *MXD2* in LAM 621-101 (*TSC2*−/−) cells knocked down with *YTHDF2* and *YTHDF3*.

(B and C) mRNA stability analysis of *MXD2* in LAM 621-101 (*TSC2*−/−) cells treated with rapamycin (100 nM) (B) or torin1 (250 nM) (C). Cells were treated with actinomycin D (5 μg/mL) for the indicated times.

(D) 5-ethynyl uridine (5-EU) labeling analysis of *MXD2* mRNA. LAM 621-101 (*TSC2*−/−) cells were labeled with 5-EU overnight and treated with rapamycin (100 nM) or torin1 (250 nM) for the indicated times.

(E) Schematic of conserved m6A RNA modification site and amino acids among various species. The consensus m6A modification motif is highlighted in yellow (GGA*C; A* is the methylated adenosine). Point mutation in m6A modification motif (C to T) is highlighted in blue.

(F and G) qPCR analysis of wild-type or m6A site-mutated *MXD2*. LAM 621-101 (*TSC2*−/−) cells were transfected with each *MXD2* construct and treated with torin1(250 nM) (F) or rapamycin (100 nM) (G) for 24 h.

n = 3. *p < 0.05, **p < 0.01, ***p < 0.001. Error bars show SD.

From our single-nucleotide-resolution m6A sequencing, we identified two mTORC1-dependent m6A sites in *MXD2* (Figure 4B; Table S1). One of these sites is highly conserved among various species (Figure 5E), indicating the functional importance of this modification. Therefore, we generated an *MXD2* mutant whose m6A modification motif is mutated without changes in amino acid sequence (Figure 5E). In contrast to wild-type *MXD2*, the expression of m6A site mutant *MXD2* was not induced by rapamycin or torin1 (Figures 5F and 5G). Collectively, these results demonstrate that mTORC1 controls *MXD2* expression via m6A modification.

WTAP induces cMyc activity and cell proliferation through MXD2

Given that mTORC1-WTAP suppresses expression of cMyc inhibitor MXD2 (Figures 4 and 5), we further investigated the impact of this signaling axis in cMyc activity and cell growth. In *WTAP* knockdown cells, expression of cMyc target genes, including *SRM*, *RPL23*, *CDC25A*, *CDC25C*, and *ODC1*, was decreased (Figures 6A and 6B) (Dang, 2012; Ji et al., 2011). Such reduction of cMyc target gene expression was fully restored by *MXD2* knockdown (Figures 6A and 6B). Mechanisti-

cally, we found that association of cMyc with MAX was decreased by *WTAP* knockdown, with concomitant increase in MXD2-MAX binding (Figure 6C) and decreased cMyc occupancy in target gene promoters (Figures S5A and S5B). *WTAP* knockdown also decreased proliferation of cancer cell lines with over-active mTORC1 signaling (Figures 6D–6I; Figures S5C–S5L), which was restored by *MXD2* knockdown (Figure 6J) and cMyc expression (Figures 6K and 6L). Notably, WTAP depletion did not significantly suppress growth of *TSC2*-restored LAM cells (Figures 2G and 6F; Figure S5C), demonstrating specific effect of WTAP in survival of mTORC1-activated cells. Therefore, MXD2-cMyc signaling is a key effector of mTORC1 and WTAP-dependent cell growth.

DISCUSSION

Here, we report that in response to growth factor stimulation, mTORC1 signaling increases the expression of m6A methyltransferase adaptor protein WTAP to induce m6A RNA modification. WTAP is an essential adaptor for the METTL3-METTL14 methyltransferase, and loss of WTAP abrogates the formation of m6A in mRNA (Ping et al., 2014; Schwartz et al., 2014). In
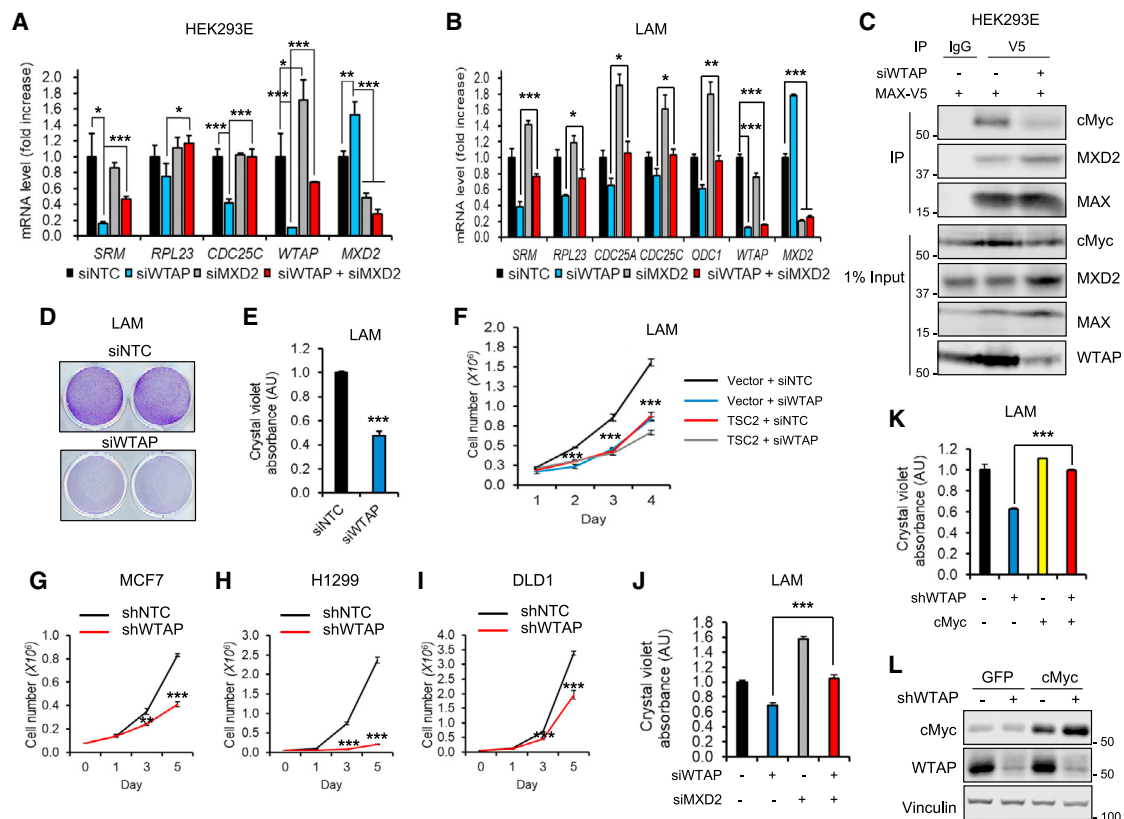
Figure 6. WTAP promotes cMyc activity and cell proliferation through MXD2

(A and B) qPCR analysis of cMyc target genes in HEK293E (A) or LAM 621-101 ($TSC2^{-/-}$) cells (B) knocked down with *WTAP* and *MXD2*.

(C) Co-immunoprecipitation analysis of MAX. HEK293E cells knocked down with *WTAP* were transfected with MAX-V5. Immunoprecipitation was performed using IgG or anti-V5 antibodies and immunoblot analysis was performed using indicated antibodies. 1% of total cell lysate was loaded as input control.

(D and E) Crystal violet (CV) staining of LAM 621-101 ($TSC2^{-/-}$) cells knocked down with *WTAP* (D). (E) shows the quantified absorbance of solubilized CV dye.

(F–I) Cell numbers were measured in LAM 621-101 ($TSC2^{-/-}$) cells expressing empty vector or *TSC2* (F), MCF7 (G), H1299 (H), or DLD1 (I) after knockdown of *WTAP*.

(J) CV staining analysis of LAM 621-101 ($TSC2^{-/-}$) cells knocked down with *WTAP* and *MXI1*. Graph shows quantified absorbance of solubilized CV dye.

(K and L) CV staining (K) and immunoblot (L) analyses of LAM 621-101 ($TSC2^{-/-}$) cells knocked down with *WTAP* with or without cMyc overexpression.

n = 3. *p < 0.05, **p < 0.01, ***p < 0.001. Error bars show SD.

addition, WTAP is required to maintain the nuclear localization and nuclear speckle enrichment of the m^{6}A writer complex, which is where methylation occurs (Ping et al., 2014). Despite the central role of WTAP in the m^{6}A writer complex, mechanisms that control its expression have not previously been identified. We show that a structured element in the *WTAP* 5′ UTR confers sensitivity to eIF4A/4B, which accounts for its translational regulation by mTORC1. Therefore, our findings indicate that controlling the level of WTAP protein is a key regulatory mechanism used by growth factors and mTORC1 to promote the m^{6}A methylation of RNA substrates during cell growth.

The cMyc transcription factor is a well-known oncogene that promotes expression of a variety of cell-growth-related genes (Dang, 2012; Ji et al., 2011). mTORC1 signaling has been shown to activate cMyc via increased transcription (Masui et al., 2013), translation (Csibi et al., 2014; West et al., 1998), and protein stabilization (Zhang et al., 2006). Our data indicate another layer of mTORC1-mediated cMyc activation by degrading the mRNA of

its suppressor, *MXD2* (Figure 7). MXD2 inhibits transcriptional activity of cMyc by preventing its binding to Max, a cMyc transcriptional co-activator (Gan et al., 2010; Schreiber-Agus et al., 1995). Expression of cMyc has also been shown to be regulated by m^{6}A methylation (Huang et al., 2018; Su et al., 2018; Vu et al., 2017). Considering the convergence of mTORC1 and cMyc activities in a variety of cellular anabolic processes (Chen et al., 2018; Pourdehnad et al., 2013), careful orchestration of cMyc expression and activity upon growth factor signaling would be critical for mTORC1-dependent cell growth and proliferation, and improper regulation is likely a major contributor to tumorigenesis.

Activation of mTORC1 signaling is detected in a majority of cancers (Lam et al., 2018; Mossmann et al., 2018). Therefore, small-molecule inhibitors targeting mTORC1, such as rapamycin and its analogs (rapalogs), have been examined for their potential efficacy against a variety of cancers. However, due to inhibition of a broad spectrum of mTORC1-regulated effectors that contribute to undesired side effects and the suppression of
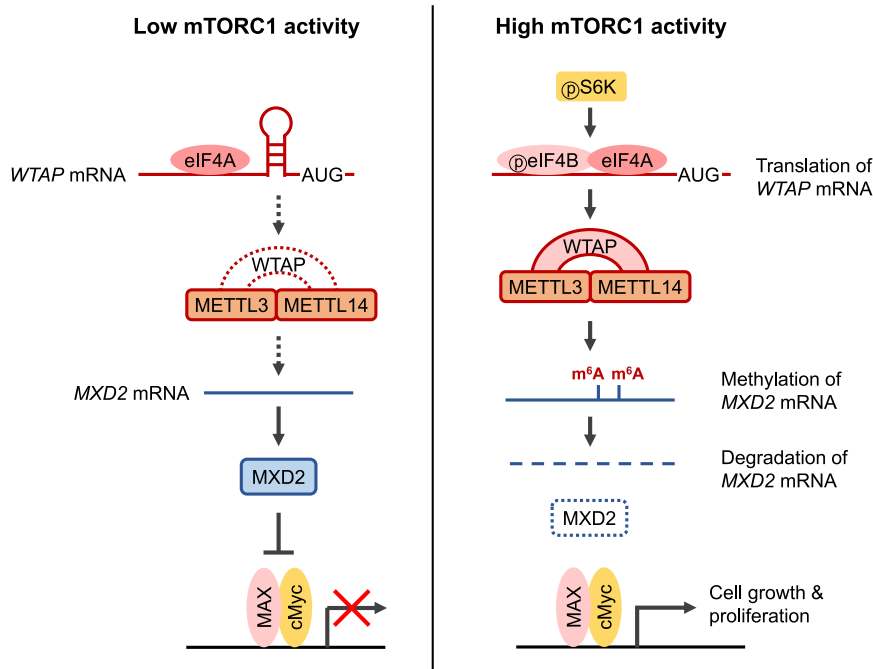
Molecular Cell
Article

CellPress

Figure 7. mTORC1 promotes cell growth by inhibiting cMyc suppressor MXD2 through m⁶A RNA modification

mTORC1 increases cellular m⁶A levels by increasing the expression of methyltransferase complex adaptor protein WTAP through eIF4A/4B-dependent translation. In cells with high mTORC1 activity, the increased m⁶A modification on *MXD2* mRNA decreases its stability, thereby suppressing MXD2 protein expression (right panel). In cells with low mTORC1-WTAP activity, MXD2 inhibits association of cMyc with its transcriptional co-activator MAX, which leads to decreased cMyc transcriptional activity and cell proliferation (left panel).

negative feedback mechanisms that normally suppress upstream inputs such as Akt signaling, rapalogs in monotherapy have had modest success in the clinic (Li et al., 2014; Sawyers, 2003). Thus, discovering new connections of this important signaling system to downstream effectors critical to the control of cell growth and survival is needed. Our data indicate that mTORC1/S6K-dependent regulation of eIF4A/4B and WTAP may provide a promising therapeutic target for mTORC1-driven cancers as well as other metabolic diseases associated with dysregulated mTORC1 signaling. Overexpression of WTAP has also been implicated in various malignancies including glioblastoma (Ji et al., 2011), leukemia (Bansal et al., 2014), and bladder (Chen and Wang, 2018), renal (Tang et al., 2018b), and liver (Chen et al., 2019) cancers. Therefore, suppression of WTAP expression using eIF4A inhibitors including silvestrol and eFT226, which are currently in preclinical and clinical trials for several types of cancers (Cunningham et al., 2018), can be a potential therapeutic approach for the treatment of mTORC1-active and WTAP-overexpressing cancers. Similarly, the recently developed small-molecule inhibitors targeting METTL3 may also hold therapeutic promise (Tzelepis et al., 2019).

Tumors rewire chemical modifications of RNAs to promote cell proliferation and survival (Barbieri and Kouzarides, 2020; Delaunay and Frye, 2019). Here, we reveal how growth factors and mTORC1 signaling regulate m⁶A RNA modification and gene expression. In support of the findings presented here, Villa et al. (2021) (this issue of *Molecular Cell*) have found that mTORC1 coordinates *S*-adenosyl methionine (SAM) production by mTORC1 to expression of WTAP and increased m⁶A levels. In addition, a second mechanism for the regulation of m⁶A has been revealed by Tang et al. (2021), which showed that mTORC1 stabilizes METTL3-METTL14 chaperonin containing TCP1 (CCT) complex. Collectively, these works provide a rationale for the

characterization of new cancer biomarkers and therapeutics targeting RNA modifications downstream of oncogenic signaling pathways.

Limitations of the study

We have found that mTORC1 regulates WTAP expression through the highly structured region in its 5′ UTR. In the current study, we have investigated this mechanism only in human and mouse systems. However, given that both mTORC1 signaling and m⁶A machineries are evolutionarily conserved from yeast to humans (Meyer and Jaffrey, 2017; Saxton and Sabatini, 2017), it will be interesting to further study whether this regulation is conserved in other species where mTORC1 and m⁶A pathways play important physiological functions. Our results demonstrate that WTAP is a major effector of mTORC1-dependent m⁶A regulation. Nevertheless, mTORC1 is known to utilize multiple layers of control in fine tuning and coordinating, from a variety of environmental inputs, the regulation of important downstream processes. One such example is the regulation of lipid metabolism. mTORC1 induces lipogenic enzymes through SREBP1/2 transcription factors by increasing SREBP expression, by regulating the proteolytic cleavage of SREBP, and by inactivating its negative regulators (Ricoult and Manning, 2013). mTORC1 also promotes mRNA splicing and stability of lipogenic enzyme transcripts (Lee et al., 2017). Furthermore, mTORC1 induces the synthesis of precursors for lipid synthesis, including acetyl-CoA and glycerol backbones, by increasing the glycolytic flux (Valvezan and Manning, 2019). Therefore, it would not be surprising and indeed makes biological sense if mTORC1 controls m⁶A modification and processing of several mRNAs through a variety of integrated and coordinated mechanisms.

STAR★METHODS

Detailed methods are provided in the online version of this paper and include the following:

● KEY RESOURCES TABLE

- RESOURCE AVAILABILITY
  - Lead Contact
  - Materials Availability
  - Data and Code Availability
- EXPERIMENTAL MODEL AND SUBJECT DETAILS
  - Cell lines and cell culture
  - Mouse studies
- METHOD DETAILS
  - Single nucleotide-resolution mapping of m^{6}A (miCLIP)
  - Bioinformatic analysis of miCLIP
  - Bioinformatics analysis
  - LC-MS analysis of m^{6}A
  - 2D-TLC analysis of m^{6}A
  - MRI imaging of mouse kidney
  - Histological analysis of kidney cystadenoma
  - Expression constructs and mutagenesis
  - CRISPR/Cas9 knockout
  - Generation of stable cell lines
  - Crystal violet staining
  - Cell growth analysis
  - Immunoblot analysis
  - Purification of RNA and proteins from tissues
  - Quantitative RT-PCR analysis
  - Polysome analysis
  - Small molecule inhibitors
  - mRNA stability assay
  - Immunoprecipitation
  - ChIP-qPCR
  - In silico analysis of 5′ UTR structure
- QUANTIFICATION AND STATISTICAL ANALYSIS

SUPPLEMENTAL INFORMATION

Supplemental information can be found online at https://doi.org/10.1016/j.molcel.2021.03.010.

AUTHOR CONTRIBUTIONS

G.L., S.C., S.R.J., and J.B. designed the study. S.C and G.L. conducted all experiments unless otherwise indicated. B.F.P. processed miCLIP samples and analyzed the results. C.J. and S.J. performed the LC-MS analysis. J.H.P., L.H., and L.M. performed some of the cellular and molecular biological experiments. S.M. provided technical assistance of histology analysis. S.-S.K. performed bioinformatics analysis. G.L., S.C., and J.B. wrote the manuscript. H.-W.T., J.D.R., and N.P. provided valuable discussions. All authors discussed the results and commented on the manuscript.

REFERENCES

Bansal, H., Yihua, Q., Iyer, S.P., Ganapathy, S., Proia, D.A., Penalva, L.O., Uren, P.J., Suresh, U., Carew, J.S., Karnad, A.B., et al. (2014). WTAP is a novel oncogenic protein in acute myeloid leukemia. Leukemia 28, 1171–1174.

Barbieri, I., and Kouzarides, T. (2020). Role of RNA modifications in cancer. Nat. Rev. Cancer 20, 303–322.

Barrilleaux, B.L., Cotterman, R., and Knoepfler, P.S. (2013). Chromatin immunoprecipitation assays for Myc and N-Myc. Methods Mol. Biol. 1012, 117–133.

Ben-Sahra, I., Hoxhaj, G., Ricoult, S.J.H., Asara, J.M., and Manning, B.D. (2016). mTORC1 induces purine synthesis through control of the mitochondrial tetrahydrofolate cycle. Science 351, 728–733.

Bordeleau, M.-E., Robert, F., Gerard, B., Lindqvist, L., Chen, S.M.H., Wendel, H.-G., Brem, B., Greger, H., Lowe, S.W., Porco, J.A., Jr., and Pelletier, J. (2008). Therapeutic suppression of translation initiation modulates chemosensitivity in a mouse lymphoma model. J. Clin. Invest. 118, 2651–2660.

Chang, J.W., Zhang, W., Yeh, H.S., de Jong, E.P., Jun, S., Kim, K.H., Bae, S.S., Beckman, K., Hwang, T.H., Kim, K.S., et al. (2015). mRNA 3′-UTR shortening is a molecular signature of mTORC1 activation. Nat. Commun. 6, 7218.

Chen, L., and Wang, X. (2018). Relationship between the genetic expression of WTAP and bladder cancer and patient prognosis. Oncol. Lett. 16, 6966–6970.

Chen, H., Liu, H., and Qing, G. (2018). Targeting oncogenic Myc as a strategy for cancer treatment. Signal Transduct. Target. Ther. 3, 5.

Chen, Y., Peng, C., Chen, J., Chen, D., Yang, B., He, B., Hu, W., Zhang, Y., Liu, H., Dai, L., et al. (2019). WTAP facilitates progression of hepatocellular carcinoma via m6A-HuR-dependent epigenetic silencing of ETS1. Mol. Cancer 18, 127.

Ciribilli, Y., and Borlak, J. (2017). Oncogenomics of c-Myc transgenic mice reveal novel regulators of extracellular signaling, angiogenesis and invasion with clinical significance for human lung adenocarcinoma. Oncotarget 8, 101808–101831.

Csibi, A., Lee, G., Yoon, S.-O., Tong, H., Ilter, D., Elia, I., Fendt, S.-M., Roberts, T.M., and Blenis, J. (2014). The mTORC1/S6K1 pathway regulates glutamine metabolism through the eIF4B-dependent control of c-Myc translation. Curr. Biol. 24, 2274–2280.

Cunningham, T.A., Chapman, E., and Schatz, J.H. (2018). eIF4A inhibition: ready for primetime? Oncotarget 9, 35515–35516.

Dang, C.V. (2012). MYC on the path to cancer. Cell 149, 22–35.

Delaunay, S., and Frye, M. (2019). RNA modifications regulating cell fate in cancer. Nat. Cell Biol. 21, 552–559.

Delpuech, O., Griffiths, B., East, P., Essafi, A., Lam, E.W.-F., Burgering, B., Downward, J., and Schulze, A. (2007). Induction of Mxi1-SR α by FOXO3a contributes to repression of Myc-dependent gene expression. Mol. Cell. Biol. 27, 4917–4930.

Dodt, M., Roehr, J.T., Ahmed, R., and Dieterich, C. (2012). FLEXBAR-Flexible Barcode and Adapter Processing for Next-Generation Sequencing Platforms. Biology (Basel) 1, 895–905.

Dominissini, D., Moshitch-Moshkovitz, S., Schwartz, S., Salmon-Divon, M., Ungar, L., Osenberg, S., Cesarkas, K., Jacob-Hirsch, J., Amariglio, N., Kupiec, M., et al. (2012). Topology of the human and mouse m6A RNA methylomes revealed by m6A-seq. Nature 485, 201–206.

Düvel, K., Yecies, J.L., Menon, S., Raman, P., Lipovsky, A.I., Souza, A.L., Triantafellow, E., Ma, Q., Gorski, R., Cleaver, S., et al. (2010). Activation of a

Molecular Cell
Article

CellPress

metabolic gene regulatory network downstream of mTOR complex 1. Mol. Cell *39*, 171–183.

Fu, Y., Dominissini, D., Rechavi, G., and He, C. (2014). Gene expression regulation mediated through reversible m⁶A RNA methylation. Nat. Rev. Genet. *15*, 293–306.

Gan, B., Lim, C., Chu, G., Hua, S., Ding, Z., Collins, M., Hu, J., Jiang, S., Fletcher-Sananikone, E., Zhuang, L., et al. (2010). FoxOs enforce a progression checkpoint to constrain mTORC1-activated renal tumorigenesis. Cancer Cell *18*, 472–484.

Gilbert, W.V., Bell, T.A., and Schaening, C. (2016). Messenger RNA modifications: Form, distribution, and function. Science *352*, 1408–1412.

Gomes, A.P., and Blenis, J. (2015). A nexus for cellular homeostasis: the interplay between metabolic and signal transduction pathways. Curr. Opin. Biotechnol. *34*, 110–117.

Gott, J.M., and Emeson, R.B. (2000). Functions and mechanisms of RNA editing. Annu. Rev. Genet. *34*, 499–531.

Hinnebusch, A.G., Ivanov, I.P., and Sonenberg, N. (2016). Translational control by 5′-untranslated regions of eukaryotic mRNAs. Science *352*, 1413–1416.

Holz, M.K., and Blenis, J. (2005). Identification of S6K1 as a novel mTOR-phosphorylating kinase. J. Biol. Chem. *280*, 26089–26093.

Holz, M.K., Ballif, B.A., Gygi, S.P., and Blenis, J. (2005). mTOR and S6K1 mediate assembly of the translation preinitiation complex through dynamic protein interchange and ordered phosphorylation events. Cell *123*, 569–580.

Huang, W., Sherman, B.T., and Lempicki, R.A. (2009). Systematic and integrative analysis of large gene lists using DAVID bioinformatics resources. Nat. Protoc. *4*, 44–57.

Huang, H., Weng, H., Sun, W., Qin, X., Shi, H., Wu, H., Zhao, B.S., Mesquita, A., Liu, C., Yuan, C.L., et al. (2018). Recognition of RNA N⁶-methyladenosine by IGF2BP proteins enhances mRNA stability and translation. Nat. Cell Biol. *20*, 285–295.

Huang, H., Weng, H., and Chen, J. (2020). m⁶A Modification in Coding and Non-coding RNAs: Roles and Therapeutic Implications in Cancer. Cancer Cell *37*, 270–288.

Jewell, J.L., and Guan, K.-L. (2013). Nutrient signaling to mTOR and cell growth. Trends Biochem. Sci. *38*, 233–242.

Ji, H., Wu, G., Zhan, X., Nolan, A., Koh, C., De Marzo, A., Doan, H.M., Fan, J., Cheadle, C., Fallahi, M., et al. (2011). Cell-type independent MYC target genes reveal a primordial signature involved in biomass accumulation. PLoS ONE *6*, e26057.

Jia, G., Fu, Y., Zhao, X., Dai, Q., Zheng, G., Yang, Y., Yi, C., Lindahl, T., Pan, T., Yang, Y.G., and He, C. (2011). N6-methyladenosine in nuclear RNA is a major substrate of the obesity-associated FTO. Nat. Chem. Biol. *7*, 885–887.

Kalogerou, M., Zhang, Y., Yang, J., Garrahan, N., Paisey, S., Tokarczuk, P., Stewart, A., Gallacher, J., Sampson, J.R., and Shen, M.H. (2012). T2 weighted MRI for assessing renal lesions in transgenic mouse models of tuberous sclerosis. Eur. J. Radiol. *81*, 2069–2074.

Kim, D.H., Sarbassov, D.D., Ali, S.M., King, J.E., Latek, R.R., Erdjument-Bromage, H., Tempst, P., and Sabatini, D.M. (2002). mTOR interacts with raptor to form a nutrient-sensitive complex that signals to the cell growth machinery. Cell *110*, 163–175.

Kimball, S.R., and Jefferson, L.S. (2006). Branched-Chain Amino Acids: Metabolism, Physiological Function, and Application Signaling Pathways and Molecular Mechanisms through which Branched-Chain Amino Acids Mediate Translational Control of Protein Synthesis. J. Nutr. *136*, 227S–231S.

Kopec, A.M., Rivera, P.D., Lacagnina, M.J., Hanamsagar, R., and Bilbo, S.D. (2017). Optimized solubilization of TRIzol-precipitated protein permits Western blotting analysis to maximize data available from brain tissue. J. Neurosci. Methods *280*, 64–76.

Kruse, S., Zhong, S., Bodi, Z., Button, J., Alcocer, M.J.C., Hayes, C.J., and Fray, R. (2011). A novel synthesis and detection method for cap-associated adenosine modifications in mouse mRNA. Sci. Rep. *1*, 126.

Lam, H.C., Siroky, B.J., and Henske, E.P. (2018). Renal disease in tuberous sclerosis complex: pathogenesis and therapy. Nat. Rev. Nephrol. *14*, 704–716.

Lasman, L., Krupalnik, V., Viukov, S., Mor, N., Aguilera-Castrejon, A., Schneir, D., Bayerl, J., Mizrahi, O., Peles, S., Tawil, S., et al. (2020). Context-dependent functional compensation between functional Ythdf m⁶A reader proteins. Genes Dev. *34*, 1373–1391.

Lee, N., Woodrum, C.L., Nobil, A.M., Rauktys, A.E., Messina, M.P., and Dabora, S.L. (2009). Rapamycin weekly maintenance dosing and the potential efficacy of combination sorafenib plus rapamycin but not atorvastatin or doxycycline in tuberous sclerosis preclinical models. BMC Pharmacol. *9*, 8.

Lee, G., Zheng, Y., Cho, S., Jang, C., England, C., Dempsey, J.M., Yu, Y., Liu, X., He, L., Cavaliere, P.M., et al. (2017). Post-transcriptional Regulation of De Novo Lipogenesis by mTORC1-S6K1-SRPK2 Signaling. Cell *171*, 1545–1558.e18.

Li, J., Kim, S.G., and Blenis, J. (2014). Rapamycin: one drug, many effects. Cell Metab. *19*, 373–379.

Lin, S., Choe, J., Du, P., Triboulet, R., and Gregory, R.I. (2016). The m⁶A Methyltransferase METTL3 Promotes Translation in Human Cancer Cells. Mol. Cell *62*, 335–345.

Linder, B., Grozhik, A.V., Olarerin-George, A.O., Meydan, C., Mason, C.E., and Jaffrey, S.R. (2015). Single-nucleotide-resolution mapping of m6A and m6Am throughout the transcriptome. Nat. Methods *12*, 767–772.

Lorenz, R., Bernhart, S.H., Höner Zu Siederdissen, C., Tafer, H., Flamm, C., Stadler, P.F., and Hofacker, I.L. (2011). ViennaRNA Package 2.0. Algorithms Mol. Biol. *6*, 26.

Ma, X.M., and Blenis, J. (2009). Molecular mechanisms of mTOR-mediated translational control. Nat. Rev. Mol. Cell Biol. *10*, 307–318.

Ma, X.M., Yoon, S.-O., Richardson, C.J., Jülich, K., and Blenis, J. (2008). SKAR links pre-mRNA splicing to mTOR/S6K1-mediated enhanced translation efficiency of spliced mRNAs. Cell *133*, 303–313.

Machanick, P., and Bailey, T.L. (2011). MEME-ChIP: motif analysis of large DNA datasets. Bioinformatics *27*, 1696–1697.

Masui, K., Tanaka, K., Akhavan, D., Babic, I., Gini, B., Matsutani, T., Iwanami, A., Liu, F., Villa, G.R., Gu, Y., et al. (2013). mTOR complex 2 controls glycolytic metabolism in glioblastoma through FoxO acetylation and upregulation of c-Myc. Cell Metab. *18*, 726–739.

Mathsyaraja, H., Freie, B., Cheng, P.F., Babaeva, E., Catchpole, J.T., Janssens, D., Henikoff, S., and Eisenman, R.N. (2019). *Max* deletion destabilizes MYC protein and abrogates Eμ-*Myc* lymphomagenesis. Genes Dev. *33*, 1252–1264.

Mauer, J., Luo, X., Blanjoie, A., Jiao, X., Grozhik, A.V., Patil, D.P., Linder, B., Pickering, B.F., Vasseur, J.-J., Chen, Q., et al. (2017). Reversible methylation of m⁶Aₘ in the 5′ cap controls mRNA stability. Nature *541*, 371–375.

Menssen, A., and Hermeking, H. (2002). Characterization of the c-MYC-regulated transcriptome by SAGE: identification and analysis of c-MYC target genes. Proc. Natl. Acad. Sci. USA *99*, 6274–6279.

Meyer, K.D., and Jaffrey, S.R. (2017). Rethinking m⁶A Readers, Writers, and Erasers. Annu. Rev. Cell Dev. Biol. *33*, 319–342.

Meyer, K.D., Saletore, Y., Zumbo, P., Elemento, O., Mason, C.E., and Jaffrey, S.R. (2012). Comprehensive analysis of mRNA methylation reveals enrichment in 3′ UTRs and near stop codons. Cell *149*, 1635–1646.

Mossmann, D., Park, S., and Hall, M.N. (2018). mTOR signalling and cellular metabolism are mutual determinants in cancer. Nat. Rev. Cancer *18*, 744–757.

Onda, H., Lueck, A., Marks, P.W., Warren, H.B., and Kwiatkowski, D.J. (1999). Tsc2(+/-) mice develop tumors in multiple sites that express gelsolin and are influenced by genetic background. J. Clin. Invest. *104*, 687–695.

Patil, D.P., Pickering, B.F., and Jaffrey, S.R. (2018). Reading m⁶A in the Transcriptome: m⁶A-Binding Proteins. Trends Cell Biol. *28*, 113–127.

Ping, X.L., Sun, B.F., Wang, L., Xiao, W., Yang, X., Wang, W.J., Adhikari, S., Shi, Y., Lv, Y., Chen, Y.S., et al. (2014). Mammalian WTAP is a regulatory subunit of the RNA N6-methyladenosine methyltransferase. Cell Res. *24*, 177–189.

Pourdehnad, M., Truitt, M.L., Siddiqi, I.N., Ducker, G.S., Shokat, K.M., and Ruggero, D. (2013). Myc and mTOR converge on a common node in protein synthesis control that confers synthetic lethality in Myc-driven cancers. Proc. Natl. Acad. Sci. USA 110, 11988–11993.

Quinlan, A.R., and Hall, I.M. (2010). BEDTools: a flexible suite of utilities for comparing genomic features. Bioinformatics 26, 841–842.

Ricoult, S.J.H., and Manning, B.D. (2013). The multifaceted role of mTORC1 in the control of lipid metabolism. EMBO Rep. 14, 242–251.

Sanjana, N.E., Shalem, O., and Zhang, F. (2014). Improved vectors and genome-wide libraries for CRISPR screening. Nat. Methods 11, 783–784.

Sarbassov, D.D., Guertin, D.A., Ali, S.M., and Sabatini, D.M. (2005). Phosphorylation and regulation of Akt/PKB by the rictor-mTOR complex. Science 307, 1098–1101.

Sawyers, C.L. (2003). Will mTOR inhibitors make it as cancer drugs? Cancer Cell 4, 343–348.

Saxton, R.A., and Sabatini, D.M. (2017). mTOR Signaling in Growth, Metabolism, and Disease. Cell 168, 960–976.

Schalm, S.S., Tee, A.R., Blenis, J., Rsprr, S.K., and Dd, D. (2005). Characterization of a conserved C-terminal (RSPRR) motif in S6K1 required for its mTOR-dependent regulation. J. Biol. Chem. 280, 11101–11106.

Schreiber-Agus, N., Chin, L., Chen, K., Torres, R., Rao, G., Guida, P., Skoultchi, A.I., and DePinho, R.A. (1995). An amino-terminal domain of Mxi1 mediates anti-Myc oncogenic activity and interacts with a homolog of the yeast transcriptional repressor SIN3. Cell 80, 777–786.

Schreiber-Agus, N., Meng, Y., Hoang, T., Hou, H., Jr., Chen, K., Greenberg, R., Cordon-Cardo, C., Lee, H.W., and DePinho, R.A. (1998). Role of Mxi in ageing organ systems and the regulation of normal and neoplastic growth. Nature 393, 483–487.

Schwartz, S., Mumbach, M.R., Jovanovic, M., Wang, T., Maciag, K., Bushkin, G.G., Mertins, P., Ter-Ovanesyan, D., Habib, N., Cacchiarelli, D., et al. (2014). Perturbation of m6A writers reveals two distinct classes of mRNA methylation at internal and 5′ sites. Cell Rep. 8, 284–296.

Shah, A., Qian, Y., Weyn-Vanhentenryck, S.M., and Zhang, C. (2017). CLIP Tool Kit (CTK): a flexible and robust pipeline to analyze CLIP sequencing data. Bioinformatics 33, 566–567.

Shahbazian, D., Parsyan, A., Petroulakis, E., Topisirovic, I., Martineau, Y., Gibbs, B.F., Svitkin, Y., and Sonenberg, N. (2010). Control of cell survival and proliferation by mammalian eukaryotic initiation factor 4B. Mol. Cell. Biol. 30, 1478–1485.

Shimobayashi, M., and Hall, M.N. (2014). Making new contacts: the mTOR network in metabolism and signalling crosstalk. Nat. Rev. Mol. Cell Biol. 15, 155–162.

Siroky, B.J., Yin, H., Babcock, J.T., Lu, L., Hellmann, A.R., Dixon, B.P., Quilliam, L.A., and Bissler, J.J. (2012). Human TSC-associated renal angiomyolipoma cells are hypersensitive to ER stress. Am. J. Physiol. Renal Physiol. 303, F831–F844.

Sommer, S., Lavi, U., and Darnell, J.E., Jr. (1978). The absolute frequency of labeled N-6-methyladenosine in HeLa cell messenger RNA decreases with label time. J. Mol. Biol. 124, 487–499.

Su, R., Dong, L., Li, C., Nachtergaele, S., Wunderlich, M., Qing, Y., Deng, X., Wang, Y., Weng, X., Hu, C., et al. (2018). R-2HG Exhibits Anti-tumor Activity by Targeting FTO/m6A/MYC/CEBPA Signaling. Cell 172, 90–105.e23.

Tang, H.W., Hu, Y., Chen, C.L., Xia, B., Zirin, J., Yuan, M., Asara, J.M., Rabinow, L., and Perrimon, N. (2018a). The TORC1-Regulated CPA Complex Rewires an RNA Processing Network to Drive Autophagy and Metabolic Reprogramming. Cell Metab. 27, 1040–1054.e8.

Tang, J., Wang, F., Cheng, G., Si, S., Sun, X., Han, J., Yu, H., Zhang, W., Lv, Q., Wei, J.-F., and Yang, H. (2018b). Wilms' tumor 1-associating protein promotes renal cell carcinoma proliferation by regulating CDK2 mRNA stability. J. Exp. Clin. Cancer Res. 37, 40.

Tang, H.-W., Weng, J.-H., Lee, W.X., Hu, Y., Gu, L., Cho, S., Lee, G., Binari, R., Li, C., Cheng, M.E., et al. (2021). mTORC1-chaperonin CCT signaling regulates m6A RNA methylation to suppress autophagy. Proc. Natl. Acad. Sci. USA 118, e2021945118.

Tzelepis, K., De Braekeleer, E., Yankova, E., Rak, J., Aspris, D., Domingues, A.F., Fosbeary, R., Hendrick, A., Leggate, D., Ofir-Rosenfeld, Y., et al. (2019). Pharmacological Inhibition of the RNA m6a Writer METTL3 As a Novel Therapeutic Strategy for Acute Myeloid Leukemia. Blood 134, 403–403.

Valvezan, A.J., and Manning, B.D. (2019). Molecular logic of mTORC1 signalling as a metabolic rheostat. Nat Metab 1, 321–333.

Valvezan, A.J., Turner, M., Belaid, A., Lam, H.C., Miller, S.K., McNamara, M.C., Baglini, C., Housden, B.E., Perrimon, N., Kwiatkowski, D.J., et al. (2017). mTORC1 Couples Nucleotide Synthesis to Nucleotide Demand Resulting in a Targetable Metabolic Vulnerability. Cancer Cell 32, 624–638.e5.

Villa, E., Sahu, U., O'Hara, B.P., Ali, E.S., Helmin, K.A., Asara, J.M., Gao, P., Singer, B.D., and Ben-Sahra, I. (2021). mTORC1 stimulates cell growth through SAM synthesis and m6A mRNA-dependent control of protein synthesis. Mol. Cell 81. Published online March 22, 2021. https://doi.org/10.1016/j.molcel.2021.03.009.

Vu, L.P., Pickering, B.F., Cheng, Y., Zaccara, S., Nguyen, D., Minuesa, G., Chou, T., Chow, A., Saletore, Y., MacKay, M., et al. (2017). The N6-methyladenosine (m6A)-forming enzyme METTL3 controls myeloid differentiation of normal hematopoietic and leukemia cells. Nat. Med. 23, 1369–1376.

Wang, X., Feng, J., Xue, Y., et al. (2016). Structural basis of N6-adenosine methylation by the METTL3–METTL14 complex. Nature 534, 575–578.

Wang, X., Lu, Z., Gomez, A., Hon, G.C., Yue, Y., Han, D., Fu, Y., Parisien, M., Dai, Q., Jia, G., et al. (2014). N6-methyladenosine-dependent regulation of messenger RNA stability. Nature 505, 117–120.

Webb, S., Hector, R.D., Kudla, G., and Granneman, S. (2014). PAR-CLIP data indicate that Nrd1-Nab3-dependent transcription termination regulates expression of hundreds of protein coding genes in yeast. Genome Biol. 15, R8.

West, M.J., Stoneley, M., and Willis, A.E. (1998). Translational induction of the c-myc oncogene via activation of the FRAP/TOR signalling pathway. Oncogene 17, 769–780.

Woodrum, C., Nobil, A., and Dabora, S.L. (2010). Comparison of three rapamycin dosing schedules in A/J Tsc2+/- mice and improved survival with angiogenesis inhibitor or asparaginase treatment in mice with subcutaneous tuberous sclerosis related tumors. J. Transl. Med. 8, 14.

Yu, J., Astrinidis, A., Howard, S., and Henske, E.P. (2004). Estradiol and tamoxifen stimulate LAM-associated angiomyolipoma cell growth and activate both genomic and nongenomic signaling pathways. Am. J. Physiol. Lung Cell. Mol. Physiol. 286, L694–L700.

Zaccara, S., and Jaffrey, S.R. (2020). A Unified Model for the Function of YTHDF Proteins in Regulating m6A-Modified mRNA. Cell 181, 1582–1595.e18.

Zhang, H.H., Lipovsky, A.I., Dibble, C.C., Sahin, M., and Manning, B.D. (2006). S6K1 regulates GSK3 under conditions of mTOR-dependent feedback inhibition of Akt. Mol. Cell 24, 185–197.

STAR★METHODS

KEY RESOURCES TABLE

REAGENT or RESOURCE	SOURCE	IDENTIFIER
Antibodies		
Rabbit monoclonal anti-cMyc	Cell Signaling Technology	Cat#5605; RRID:AB_1903938
Rabbit polyclonal anti-S6K1	Cell Signaling Technology	Cat#2708; RRID: AB_390722
Rabbit monoclonal anti-pS6(S240/S244)	Cell Signaling Technology	Cat#5364; RRID: AB_10694233
Rabbit monoclonal anti-mTOR	Cell Signaling Technology	Cat#5048; RRID:AB_10828101
Rabbit monoclonal anti-Raptor	Cell Signaling Technology	Cat#2280; RRID:AB_561245
Rabbit polyclonal anti-Rictor	Cell Signaling Technology	Cat#9476; RRID:AB_10612959
Rabbit anti-eIF4A1	Cell Signaling Technology	Cat#2490; RRID:AB_823487
Rabbit anti-eIF4B	Cell Signaling Technology	Cat#3592; RRID:AB_2293388
Rabbit monoclonal anti-TSC2	Cell Signaling Technology	Cat#4308; RRID:AB_10547134
Rabbit polyclonal anti-METTL3	Proteintech	Cat#15073-1-AP; RRID:AB_2142033
mouse monoclonal anti-Vinculin	Sigma-Aldrich	Cat#V9264; RRID: AB_10603627
Rabbit polyclonal anti-METTL14	Sigma-Aldrich	Cat#HPA038002; RRID:AB_10672401
Rabbit polyclonal anti-MXD2	Sigma-Aldrich	Cat#HPA035319; RRID:AB_10670588
Mouse monoclonal anti-WTAP	Proteintech	Cat#60188-1-Ig; RRID:AB_10859484
Rabbit anti-WTAP	Abcam	Cat#ab195380; RRID:AB_2868572
Rabbit anti-WTAP	Novus	Cat#NBP1-83040; RRID:AB_11041336
Rabbit polyclonal anti-S6K2	Gene Tex	Cat#GTX101886; RRID:AB_1951783
Mouse monoclonal anti-HA	Santa Cruz Biotechnology	Cat#sc-7392; RRID:AB_627809
Rabbit polyclonal anti-cMyc (ChIP)	Cell Signaling Technology	Cat#9402; RRID:AB_2151827
Rabbit polyclonal anti-MAX	Bethyl	Cat#A302-866A; RRID:AB_10634559
Rabbit polyclonal Anti-N6-methyladenosine (m6A) antibody	Abcam	Cat#ab151230; RRID:AB_2753144
Rabbit Normal IgG	Cell Signaling Technology	Cat#2729; RRID:AB_1031062
Chemicals, Peptides, and Recombinant Proteins		
Anti-Flag agarose affinity gel	Sigma-Aldrich	Cat#A2220
Rapamycin	Calbiochem	Cat#553210
Rapamycin	LC Laboratories	Cat#R-5000
PF4708671	Sigma-Aldrich	Cat#PZ0143
Torin1	Tocris Bioscience	Cat#4247
Actinomycin D	Sigma-Aldrich	Cat#A1410
RNase inhibitor	Invitrogen	Cat#10777019
Anti-V5 agarose affinity gel	Sigma-Aldrich	Cat#A7345
Lipofectamine RNAiMAX Transfection Reagent	Invitrogen	Cat#13778075
Lipofectamine 3000 reagent	Invitrogen	Cat#L3000015
DNase I	Sigma-Aldrich	Cat#AMPD1
$[\gamma\text{-}^{32}P]$-ATP	Perkin Elmer	Cat#NEG035C001MC
RNA Fragmentation Reagents	Thermo Fisher Scientific	Cat#AM8740
T4 Polynucleotide Kinase	New England Biolabs	Cat#M0201S
Apyrase	New England Biolabs	Cat#M0398L
TRIzol	Invitrogen	Cat#15596018
Protein A/G magnetic beads	Thermo Fisher Scientific	Cat#88802
Proteinase K	New England Biolabs	Cat#P8107
Lipofectamine 2000 reagent	Invitrogen	Cat#11668500
NuPAGE 4-12% Bis Tris Protein Gels	Thermo Fisher Scientific	Cat#NP0321BOX

Continued

REAGENT or RESOURCE	SOURCE	IDENTIFIER
Phenol:Chloroform:IAA, 25:24:1, pH 6.6	Thermo Fisher Scientific	Cat#AM9730
SuperScript IV Reverse Transcriptase	Invitrogen	Cat#18090010
Circligase I	Lucigen	Cat#CL4111K
AMPure XP for PCR Purification	Beckman Coulter	Cat#A63880
Nuclease P1 from Penicillium citrinum	Sigma-Aldrich	Cat#N8630-1VL
Phosphatase, Alkaline from *Escherichia coli*	Sigma-Aldrich	Cat#P5931-100UN
TLC PEI Cellulose F	Merck-Millipore	Cat#105725
Silvestrol	Cheme scene	Cat#CS-0543
Insulin solution human	Sigma-Aldrich	Cat#I9278
Crystal Violet	Sigma-Aldrich	Cat#C3886
Oligo d(T)$_{25}$ Magnetic Beads	New England Biolabs	Cat#S1419S
Dynabeads Oligo(dT)$_{25}$	Invitrogen	Cat#61005
10% neutral buffered formalin	RICCA Chemical	Cat#3190-1
Methanol-free 10% formaldehyde	Polysciences	Cat#04018-1
Cycloheximide	Sigma-Aldrich	Cat#C4859
Critical Commercial Assays		
PureLink RNA Mini kit	Ambion	Cat#12183018A
iScript cDNA synthesis kit	Bio-rad	Cat#170-8891BUN
High-Capacity cDNA Reverse Transcription Kit	Applied Biosystems	Cat#4368814
KAPA HiFi HotStart Library Amplification Kit Illumina Platforms	Kapa Biosystems	Cat#KR0408
Gateway LR clonase II enzyme mix	Invitrogen	Cat#11791
QuickChange site-directed mutagenesis kit	Strategene	Cat#200521
RNA Clean & Concentrator	Zymo Research	Cat#R1016
Click-it Nascent RNA Capture Kit	Thermo Fisher Scientific	Cat#C10365
ChIP-IT Express Kit	Active Motif	Cat#53009
Chromatin IP DNA purification kit	Active Motif	Cat#58002
SYBR Green PCR Master Mix	Life Technologies	Cat#4312704
TuRboCapture 96 mRNA Kit	QIAGEN	Cat#72251
Deposited Data		
Raw miCLIP data	This paper	GSE152633
Raw data of Images and WB	This paper, Mendeley Data	http://dx.doi.org/10.17632/7sgjcvjpt9.2
Experimental Models: Cell Lines		
Human: Renal angiomyolipoma-derived LAM 621-101 (*TSC2*−/−)	Drs. Jane Yu and Elizabeth Henske	Yu et al., 2004
Human: HEK293E	ATCC	Cat#293 c18; RRID: CVCL_6974
Human: HEK293T	GenHunter	Cat#Q401
Human: MCF7	ATCC	Cat#HTB-22; RRID: CVCL_0031
Human: DLD1	ATCC	Cat#CCL-221; RRID: CVCL_0248
Human: NCI-H1299	ATCC	Cat#CRL-5803; RRID: CVCL_0060
Human: BT549	ATCC	Cat#HTB-122; RRID:CVCL_1092
Experimental Models: Organisms/Strains		
Male *Tsc2*$^{tm1Djk/+}$ mice (A/J strain)	Tuberous Sclerosis Alliance and Van Andel Institute	Onda et al., 1999
Male wild-type A/J strain mice	Jackson Laboratory	Cat#000646
Oligonucleotides		
pLKO.1-puro-Non-Mammalian shRNA Control	Sigma-Aldrich	SHC002
pLKO.1-puro-shWTAP-#1(Human)	Sigma-Aldrich	TRCN0000231426
pLKO.1-puro-shWTAP-#2(Human)	Sigma-Aldrich	TRCN0000001074

Molecular Cell
Article

🔗 **CellPress**

Continued

REAGENT or RESOURCE	SOURCE	IDENTIFIER
pLKO.1-puro-shWTAP-#3(Human)	Sigma-Aldrich	TRCN0000231422
sgRNA targeting sequence (Human WTAP): CTGACAAACGGACCAAGTAA	This paper	N/A
Primers for qPCR analysis, see Table S3	This paper	N/A
siRNAs list, see Table S4	This paper	N/A
Recombinant DNA		
pcDNA3-Flag-METTL3	Addgene	Cat#53739
pcDNA3-Flag-METTL14	Addgene	Cat#53740
pCDNA3-HA-human cMYC	Addgene	Cat#74164
Lentiviral packaging and envelope plasmids	Dr. David Baltimore	N/A
pcDNA3-EGFP	Addgene	Cat#13031
pDONR223-MAX-WT-V5	Addgene	Cat#82944
pcDNA3-MXD2	Dr. AlmutSchulze	Delpuech et al., 2007
lentiCRISPRv2 vector	Dr. Feng Zhang	Sanjana et al., 2014
pKH3-S6K1-F5A/T389E/R3A	Dr. John Blenis	Schalm et al., 2005
pENTR-WTAP(5′ UTR+CDS)	This paper	N/A
pcDNA3-Flag-WTAP(CDS)	Addgene	Cat#53741
pcDNA3-METTL3-D395A/W398A	This paper	N/A
pcDNA3-MXD2-C882T(m⁶A site mutant)	This paper	N/A
Software and Algorithms		
FLEXBAR	Dodt et. al., 2012	https://github.com/seqan/flexbar/wiki
MEME-ChIP de novo motif search	Machanick and Bailey 2011	https://www.ncbi.nlm.nih.gov/pubmed/21486936
CTK package	Shah et al., 2017	https://github.com/chaolinzhanglab/ctk
BEDTools	Quinlan and Hall, 2010	https://github.com/arq5x/bedtools2
Adobe Photoshop	Adobe	Adobe
Odyssey imaging system	LI-COR Biosciences	LI-COR Biosciences
pyCRAC.py	Webb et al., 2014	https://git.ecdf.ed.ac.uk/sgrannem/pycrac
DAVID	Open source	http://david.abcc.ncifcrf.gov/
Other		
Mass spectrometry	Dr. Joshua Rabinowitz and Dr. Cholsoon Jang	N/A
MRI imaging (9.4T 20-cm bore Bruker Biospec scanners)	Memorial Sloan Kettering Cancer Center	N/A

RESOURCE AVAILABILITY

Lead Contact
Further information and requests for resources and reagents should be directed to and will be fulfilled by the Lead Contact, John Blenis (job2064@med.cornell.edu).

Materials Availability
All reagents generated in this study are available from the Lead Contact without restriction.

Data and Code Availability
The image dataset supporting the current study have been deposited in a public repository; Mendeley Data: http://dx.doi.org/10.17632/7sgjcvjpt9.2. The miCLIP-seq and RNA-seq data files dataset generated in this study is available at GEO: GSE165690. These datasets can be found at https://www.ncbi.nlm.nih.gov/geo/query/acc.cgi?acc=GSE152633 using the following token: uzghcsuafjknzwt.

EXPERIMENTAL MODEL AND SUBJECT DETAILS

Details of cell lines used have been provided under section "Cell lines and cell culture" and details of mice used have been provided under "Mouse studies."

Cell lines and cell culture

HEK293E and HEK293T cells were obtained from ATCC and GenHunter, respectively. Human renal angiomyolipoma-derived LAM 621-101 cells stably expressing empty vector or TSC2 were provided by Elisabeth Henske (Siroky et al., 2012). BT549, DLD1, MCF7, and NCI-H1299 cells were obtained from ATCC. HEK293E, HEK293T, NCI-H1299, BT549, and LAM 621-101 Cells were grown in DMEM (GIBCO) with 10% FBS (Sigma-Aldrich-Aldrich) at 37°C with 5% CO$_2$. MCF7, and DLD1 cells were cultured in RPMI (Corning) with 10% FBS (Sigma-Aldrich-Aldrich).

Mouse studies

All animal procedures were approved by the Institutional Animal Care and Use Committee (IACUC) at Weill Cornell Medicine. Nine-month-old male *Tsc2$^{tm1Djk/+}$* mice on the A/J strain background (referred to as *Tsc2$^{+/-}$* in this article) (Onda et al., 1999; Woodrum et al., 2010) were provided by Tuberous Sclerosis Alliance and Van Andel Institute. Wild-type male A/J strain mice of a similar age were obtained from the Jackson Laboratory (Stock No. 000646). Rapamycin (LC Laboratories) was dissolved in DMSO as 20 mg/mL stock. The stock solution was freshly diluted with vehicle (0.25% Polyethylene Glycol and 0.25% Tween-80) for the treatment. Intraperitoneal injection of vehicle or rapamycin (8 mg/kg) was administered every other day for 8 weeks at the beginning of 11-month of age. MRI was taken before (0 week) and after (8 week) the drug treatment to detect kidney cystadenomas.

METHOD DETAILS

Single nucleotide-resolution mapping of m^{6}A (miCLIP)

m^{6}A mapping was performed as previously described (Linder et al., 2015). Briefly, 15 μg of twice poly(A) purified RNA from HEK293E cells (samples in biological triplicate) was sheared using an RNA fragmentation reagent (Thermo Fisher Scientific) at 70°C for 7 min. 150 ng of each sample was saved as input for RNA-seq. Samples were then incubated with 15 μg of anti-m^{6}A antibody (Abcam ab151230) for 2 h at 4°C and then UV crosslinked twice at 150 mJ × sec^{-1}/cm^2. Following one-h incubation with Protein A/G magnetic beads (Thermo Fisher Scientific), the beads were extensively washed as previously described. After washing, 3′ ends were dephosphorylated with T4 Polynucleotide Kinase (PNK, New England Biolabs) and pre-adenylated adapters were ligated to the 3′ end. Samples were radiolabeled with γ-^{32}P-ATP (Perkin Elmer) and PNK, run on a 4%–12% Bis-Tris NuPAGE gel (Thermo Fisher Scientific) and transferred to 0.45 μm a nitrocellulose membrane. RNA was liberated from the membrane using proteinase K (New England Biolabs) in 50 mM Tris [pH 7.4], 100 mM NaCl, 0.5% SDS, 1 mM EDTA at 50°C for one h. Samples were then phenol:chloroform (Thermo Fisher Scientific) extracted and ethanol precipitated. Barcoded reverse transcription primers with unique molecular identifier barcodes were annealed to adaptor sequences and reverse transcribed using Superscript IV (Invitrogen). The resulting cDNA was gel purified and eluted overnight at 37°C. cDNA was then circularized using Circligase I (Lucigen) for 8 h at 60°C. Libraries were amplified using KAPA HiFi (Kapa Biosystems) and primers removed with Ampure XP beads (Beckman Coulter). Paired-end 50 nucleotide reads were sequenced using a HiSeq 2500 at the Weill Cornell Medicine Epigenomics Core Facility.

Bioinformatic analysis of miCLIP

Analysis of miCLIP reads was performed as previously described (Linder et al., 2015). First, adaptor sequences were removed using Flexbar (–pre-trim-phred 30) and demultiplexed using pyBarcodeFilter.py (Dodt et al., 2012). PCR duplicates were removed using pyCRAC.py (Webb et al., 2014). The forward and reverse-complement reverse reads were concatenated and aligned using Burrow-Wheeler Aligner (bwa aln -n 0.06 -q 20 GRCh38/hg38.fa). Single-nucleotide m^{6}A sites were called using CIMS.pl in the CTK package (Shah et al., 2017). High-confidence m^{6}A sites were called by filtering adenosines followed by a C®T transition with a p value < 0.05 that fell within a DRACH consensus sequence. Unique m^{6}A sites from biological triplicates were pooled for meta-gene analysis and motif analysis using MEME-CHIP (Machanick and Bailey, 2011). Coverage at m^{6}A sites was determined by first normalizing library sizes to the number of unique transcripts per million reads (uTPM). Read coverage at m^{6}A sites was determined using BEDTools Coverage (Quinlan and Hall, 2010). For cumulative distribution plot, the number of m^{6}A sites for transcripts in control (DMSO treated) cells was calculated and used to determine log$_2$ fold-change for input RNA-seq following binning transcripts based on the number of m^{6}A sites.

Bioinformatics analysis

For the gene ontology (GO) enrichment analysis (Table S1 and 2), the list of genes was uploaded to the DAVID database website (https://david.ncifcrf.gov/) for biological pathway analysis.

Molecular Cell
Article

CellPress

LC-MS analysis of m^{6}A

Total RNA was isolated by Purelink RNA miniprep kit (Ambion) or Trizol (Invitrogen). Poly(A) RNAs were purified by Oligo(dT) beads (Thermo Fisher Scientific or NEB) and RNA clean up kit (Zymo Research). 100-200 ng of twice-purified poly(A)-RNA was digested with 1 unit of nuclease P1 (Sigma-Aldrich) for 2 h at 37°C followed by 1 unit of alkaline phosphatase (Sigma-Aldrich) treatment for 2 h at 37°C. Adenosine and m^{6}A levels were analyzed by quadrupole-time of flight mass spectrometer (Q-TOF, Agilent) or quadrupole-orbitrap mass spectrometer (Q-Exactive Plus Hybrid Quadrupole-Orbitrap, Thermo Fisher) mass spectrometers. Q-TOF operating in positive ion mode was coupled to C18 chromatography via electrospray ionization and used to scan from m/z 200 to 300 at 1 Hz and 15,000 resolution. LC separation was on an Acquity UPLC BEH C18 column (2.1 mm x 100 mm, 1.75 μm particle size, 130 Å pore size; Waters) at 60°C using a gradient of solvent A (100% water) and solvent B (100% methanol). Flow rate was 400 μL/min, except that from 6 min to 8 min flow rate was increased to 700 μL/min. The LC gradient was: 0 min, 10% B; 1 min, 10% B; 5 min, 30% B; 7 min, 100% B; 11 min, 100% B; 11.5 min, 10% B; 14 min, 10% B. Q-Exactive operating in positive ion mode was coupled to hydrophilic interaction chromatography (HILIC) via electrospray ionization and used to scan from m/z 250 to 300 and 140,000 resolution. LC separation was on an Xbridge BEH amide column (2.1 mm x 150 mm, 2.5 μm particle size, 130 Å pore size; Waters) at 25°C using a gradient of solvent A (5% acetonitrile in water with 20 mM ammonium acetate and 20 mM ammonium hydroxide) and solvent B (100% acetonitrile). Flow rate was 350 μL/min. The LC gradient was: 0 min, 75% B; 3 min, 75% B; 4 min, 50% B; 5 min, 10% B; 7 min, 10% B; 7.5 min, 75% B; 11 min, 75% B.

2D-TLC analysis of m^{6}A

Two-dimensional thin-layer chromatography (2D-TLC) analysis of m^{6}A levels on mRNA was performed as described previously (Kruse et al., 2011). Briefly, 100 ng of twice-purified poly(A)-RNA was digested with 2 units of ribonuclease T1 for 2 h at 37°C with RNase inhibitor (Invitrogen). Digested mRNA was labeled with ^{32}P-ATP by incubating the digested mRNAs with T4 PNK (10 units, NEB) and 0.4 mBq [γ-^{32}P] ATP (PerkinElmer) for 30 min at 37°C. After labeling, 10 units of apyrase (NEB) was added for 30 min at 30°C to hydrolyze γ-phosphate from free ^{32}P-ATP. After phenol:chloroform extraction and ethanol precipitation, samples were resuspended in 8 μl of nuclease-free water and incubated with 1 unit of nuclease P1 for 3 h at 37°C. The nucleotides were then spotted on the glass-backed PEI-cellulose plates (Merck-Millipore) and separated by two different separation stages as described previously (Mauer et al., 2017). The plates were exposed to a storage phosphor screen (GE Healthcare Life Sciences) and processed on a Typhoon Trio imager (GE Healthcare Life Sciences). Imagestudio software (Li-Cor) was used to quantify the intensity of individual spots. The relative amount of m^{6}A was measured as a percentage of the total intensity of A, C and U spots, as described previously (Mauer et al., 2017).

MRI imaging of mouse kidney

MRI scans were performed at the Animal Imaging Core Facility at Memorial Sloan Kettering Cancer Center (MSKCC) using a 9.4T 20-cm bore Bruker Biospec scanners (Bruker Biospin MRI GmbH, Ettlingen) equipped with an ID 114 mm maximum strength of 530 mT/m Bruker gradient. An ID 40 mm Bruker volume resonator was used for RF excitation and MRI signal acquisition. The mice were anesthetized with 2% isoflurane gas (Baxter Healthcare Corporation) in oxygen. Animal respiration was monitored with a small animal physiological monitoring system (SA Instruments). To image kidney area, respiratory coronal T2-weighted images were acquired using fast spin-echo Rapid Acquisition with Relaxation Enhancement (RARE) sequence (TR 2.0 s, TE 33 ms, RARE factor of 8, slice thickness of 0.4 mm, FOV 30 mm, in-plane resolution of 117 um, and 10 averages). Kidney cystadenomas in the MRI images were categorized as cyst (white spots), papillary (partially filled gray spots), and solid tumors (gray spots) as previously described (Kalogerou et al., 2012; Lee et al., 2009).

Histological analysis of kidney cystadenoma

After 8 weeks of drug treatment, mice were euthanized by carbon dioxide (CO_2). Kidneys were fixed with 10% neutral buffered formalin (RICCA Chemical) for 48 h and transferred to 70% ethanol. The fixed tissues were sliced sagitally, processed in alcohol and xylene, and paraffin-embedded following standard procedures. Slides were prepared with a series of 5 μm coronal sections taken at 700 μm intervals. Slides were hematoxylin and eosin (H&E) stained, and whole-slide images were generated on a slide scanner (Pannoramic 250 Flash III, 20x/0.8NA objective, 3DHistech) at a pixel size of 0.2431 μm per pixel. Images were analyzed and annotated using Caseviewer 2.2 software (3D Histech) by blinded researchers, including a board-certified veterinary pathologist (SM). Lesions were scored semiquantitatively using a previously described method (Lee et al., 2009). Briefly, the tumor score was calculated by the sum of the tumor lesion scores per kidney according to the tumor lesion area. Tumor lesion score (mm^2): 0 (0), 1 (0 < x £ 0.09), 2 (0.09 < x £ 0.2), 3 (0.2 < x £ 0.35), 4 (0.35 < x £ 0.5), 5 (x > 0.5).

Expression constructs and mutagenesis

Expression constructs were transfected using Lipofectamine 2000 or 3000 reagent (Invitrogen). METTL3 (Addgene plasmid 53739), METTL14 (Addgene plasmid 53740), cMyc (Addgene plasmid, 74164), GFP (Addgene plasmid 13031), or Max (Addgene plasmid, 82944) were obtained from Addgene. The human MXD2 plasmid, cloned into pcDNA 3, was a gift from Dr. Almut Schulze (German Cancer Research Center, Germany) (Delpuech et al., 2007). To generate WTAP expression plasmids, the coding sequence of human WTAP with or without 5′ UTR (Genbank: NM_004906.4) was cloned into pENTR vector, and pLenti-blasticidin-based plasmids were

generated by Gateway LR reaction (Invitrogen). The constitutively active S6K1 (pKH3-S6K1-F5A/T389E/R3A) is previously described (Csibi et al., 2014; Schalm et al., 2005). 15-30 nM siRNAs (Sigma-Aldrich-Aldrich) were transfected using Lipofectamine RNAiMAX reagent (Invitrogen): Negative control (SIC001, SIC002), METTL3 (SASI_Hs01_00044317, SASI_Hs01_00044318, SASI_Hs01_00044319, SASI_Hs01_00044320), METTL14 (SASI_Hs01_00179440, SASI_Hs01_00179441, SASI_Hs02_00354390, SASI_Hs01_00179442), WTAP (SASI_Hs01_00039282, SASI_Hs01_00039283, SASI_Hs01_00039284, SASI_Hs01_00102839, SASI_Hs01_00102842), YTHDF2 (SASI_Hs01_00133214, SASI_Hs01_00133215), YTHDF3 (SASI_Hs01_00202277, SASI_Hs01_00202278), mTOR (SASI_Hs01_00203144, SASI_Hs01_00203145), Raptor (SASI_Hs01_00048380, SASI_Hs01_00048381, SASI_Hs01_00048382), Rictor (SASI_Hs01_00223573, SASI_Hs01_00223574, SASI_Hs01_00366683), S6K1 (SASI_Hs01_00148595, SASI_Hs01_00148596, SASI_Hs01_00148597), S6K2 (SASI_Hs01_00218651, SASI_Hs01_00218652, SASI_Hs01_00218653), eIF4A1 (SASI_Hs02_00331809, SASI_Hs02_00331808), eIF4A2 (SASI_Hs01_00119368, SASI_Hs01_00119367), eIF4B (SASI_Hs01_00121466, SASI_Hs02_00331818), and MXD2 (SASI_Hs01_00139543, SASI_Hs01_00139544, SASI_Hs01_00139545). shRNA construct was obtained from the RNAi Consortium (TRC) at the Broad Institute: shWTAP (TRCN0000231426, targeting 3′ UTR; TRCN0000001074 and TRCN0000231422, targeting CDS). Non-mammalian targeting control shRNA (shNTC) was obtained from Sigma-Aldrich-Aldrich (Sigma-Aldrich-Aldrich, SHC002). METTL3 catalytic dead mutant METTL3-D395A/W398A (A1184C/TG1192GC) and MXD2 m⁶A site mutant (C882T) were generated using QuickChange site-directed mutagenesis kit (Strategene).

CRISPR/Cas9 knockout
Guide RNA sequence against human WTAP (CTGACAAACGGACCAAGTAA) was cloned into lentiCRISPRv2 vector (Sanjana et al., 2014). HEK293T cells were co-transfected with lentiCRISPRv2 construct, lentiviral packaging, and envelope plasmids to generate virus. HEK293E cells were infected with viral supernatants with polybrene (8 μg/mL) and selected with puromycin (2 μg/mL). After selection, cells were serial diluted in 96-well plates to isolate single cell clone of WTAP knockout cells, followed by immunoblot analysis of WTAP to confirm knockout efficiency.

Generation of stable cell lines
To generate lentiviruses, HEK293T cells were co-transfected with the viral plasmid of interest with packaging and envelope plasmids using Lipofectamine 2000. The next day media was changed, and virus-containing supernatants were collected at 48 h after transfection. Target cells were infected with 0.45 μM-filtered viral supernatants in the presence of a serum-containing medium supplemented with 8 μg/mL polybrene for 16 h. After 16 h, viral-containing medium was removed and cells were grown in serum-containing medium for 24 h. Virus infected cells were treated with puromycin (2 μg/mL) for selection. The knockdown of target protein was confirmed by immunoblot or qPCR analysis.

Crystal violet staining
Cells were fixed with 4% methanol-free formaldehyde (Polysciences) and incubated with 0.1% crystal violet solution (Sigma-Aldrich-Aldrich) for 30 min. After rinsing five times with PBS, the plates were scanned for image analysis. For quantification, dyes were eluted using methanol, and the absorbance of crystal violet solutions was measured at 570 nm using Envision plate reader (PerkinElmer).

Cell growth analysis
Cells seeded on 6-well plates (LAM 621-101, 1×10^5 cells; MCF7, 8×10^4 cells; H1299 and DLD1, 5×10^4 cells) were grown in the media (MCF7 and DLD1, RPMI; LAM 621-101 and H1299, DMEM) with 10% FBS. Cell numbers were counted on the indicated day using Multisizer 3 Coulter Counter (Beckman Coulter).

Immunoblot analysis
Cells were homogenized on ice either using RIPA (40 mM HEPES [pH 7.4], 1 mM EDTA, 120 mM NaCl, 0.5 mM DTT, 0.1% Brij-35, 0.1% deoxycholate, 0.5% NP-40) or Triton X-100 (40 mM HEPES [pH 7.4], 1 mM EDTA, 120 mM NaCl, 0.5 mM DTT, 1% Triton X-100) lysis buffers supplemented with protease inhibitors (250 μM PMSF, 5 μg/mL pepstatin A, 10 μg/mL leupeptin, 5 μg/mL aprotinin) and phosphatase inhibitors (10 mM β-glycerophosphate, 1 mM NaF, 1 mM Na₃VO₄). Cell lysates were cleared by centrifugation at 13,000 rpm at 4°C for 30 min. Bradford protein assay or detergent compatible (DC) protein assay (Bio-rad) was used to measure protein concentration. Proteins were boiled for 10 min with Laemmli sample buffer. SDS-PAGE gels were used to separate proteins (15-60 μg) and transferred to nitrocellulose membrane (Amersham Biosciences). Membranes were then incubated with Odyssey blocking solution (LI-COR Biosciences), followed by incubation with primary and IRDye secondary (LI-COR Biosciences) antibodies. Immunoblot signals were detected and quantified by Odyssey imaging system (LI-COR Biosciences). Immunoblot images are representative of at least two independent experiments. Antibodies against cMyc, pS6(S240/S244), S6K1, mTOR, Raptor, Rictor, eIF4A1, eIF4B, and TSC2 (Cell Signaling Technology); METTL3 (Proteintech); METTL14, MXD2, and Vinculin (Sigma-Aldrich-Aldrich); WTAP (Proteintech and Abcam for human; Novus for mouse); S6K2 (Genetex); MAX (Bethyl); and HA (Santa Cruz) were used.

Purification of RNA and proteins from tissues
Simultaneous isolation of RNA and protein from tissues was performed following the protocol in Kopec et al. (Kopec et al., 2017). Briefly, tissues were lysed with Trizol (Invitrogen) and homogenized using a tissuelyser (QIAGEN). After adding chloroform, the top

Molecular Cell
Article

CellPress

layer of the aqueous solution was processed for RNA purification following the manufacturer's protocol. For purification of proteins, 100% ethanol was added to the bottom layer of the aqueous solution. After centrifugation, isopropanol was added to the supernatant to precipitate proteins. Protein pellet was washed with 95% ethanol and dissolved in lysis buffer (20 mM EDTA,140 mM NaCl, 5% SDS, 100 mM Tris [pH 8.0]).

Quantitative RT-PCR analysis
PureLink RNA isolation kit (Life Technologies) or Trizol (Invitrogen) was used to isolate total RNA from cells and tissues. Genomic DNA was removed by DNase I (Sigma-Aldrich-Aldrich) treatment. RNA was reverse transcribed using iScript kit (Bio-rad) unless otherwise indicated. The resulting cDNA was analyzed by quantitative RT-PCR (qPCR) using SYBR green master mix (Life Technologies) on QuantStudio6 Real-Time PCR system (Life Technologies). mRNA levels were calculated by delta-delta CT method using house-keeping genes ACTIN, GAPDH, PPIB, and TBP (human); or Actin, Tbp and, 36b4 (mouse) as controls. Primer list is in Table S3.

Polysome analysis
After treatment of 100 μg/mL cycloheximide (Sigma-Aldrich-Aldrich) for 5 min, cells were washed twice with ice-cold PBS containing 100 μg/mL cycloheximide and solubilized by polysome lysis buffer (15 mM Tris [pH 7.4], 15 mM MgCl$_2$, 250 mM NaCl, 1% Triton X-100, 1 mM DTT, 100 μg/mL cycloheximide, 400 U/mL RNaseOut (Invitrogen), protease inhibitors). Lysates were centrifuged for 15 min at 13,000 rpm at 4°C. Cell lysates containing the same amount of total RNAs were loaded onto 20% to 50% sucrose gradient generated by Gradient Station (Biocomp). Tubes were centrifuged at 36,000 rpm for 2 h at 4°C on SW40Ti rotor (Beckman Coulter). After centrifugation, fractions were collected using Foxy JR Fraction Collector and UA-6 Absorbance Detector (Teledyne Isco). RNA was extracted using TurboCapture 96 mRNA Kit (QIAGEN) and reverse transcribed using High-Capacity cDNA Reverse Transcription Kit (Applied Biosystems). mRNA levels in the resulting cDNA were analyzed by qPCR.

Small molecule inhibitors
Insulin, PF4708671, actinomycin D, and cycloheximide (Sigma-Aldrich-Aldrich); Torin1 (Tocris Bioscience); Rapamycin (Calbiochem and LC Laboratories); and Silvestrol (ChemScene).

mRNA stability assay
Actinomycin D (5 μg/mL) was treated to cells for the indicated times, and the mRNA levels at each time point were analyzed by qPCR. For 5-ethynyl uridine labeling, 5-ethynyl uridine (0.2 mM) was added to the complete culture medium for overnight and washed with PBS twice and harvested the samples for 0 h and other cells were treated with rapamycin (100 nM) or torin1 (250 nM) for 24 h. Total RNA was isolated by Purelink RNA miniprep kit (Ambion), and EU labeled RNAs were isolated using a commercially available kit (Click-iT Nascent RNA Capture Kit, life technologies).

Immunoprecipitation
Cells on a 10-cm plate were washed twice with ice-cold PBS and harvested into 15 mL tube. Cells were collected by centrifugation at 1,000 x g at 4°C for 5 min. Cell pellets were re-su spended with 1 mL of lysis buffer (20 mM Tris HCl pH 8, 137 mM NaCl, 1% Nonidet P-40, 2 mM EDTA) supplemented with protease inhibitors (250 μM PMSF, 5 μg/mL pepstatin A, 10 μg/mL leupeptin, 5 μg/mL apro-tinin) and phosphatase inhibitors (10 mM β-glycerophosphate, 1 mM NaF, 1 mM Na$_3$VO$_4$), and incubated on ice for 30 min. After centrifugation at 13,000 rpm at 4°C for 30 min, 1mg of lysates were incubated with anti-V5 (Sigma-Aldrich) or anti-Flag agarose af-finity gels (Sigma-Aldrich) to pull down immune complexes for 1.5 h at 4°C. Beads were washed with lysis buffer for 3 times and were boiled with 2X Laemmli sample buffer for 10 min. Boiled beads were briefly centrifuged and supernatants were subjected to immu-noblot analysis.

ChIP-qPCR
Cells were fixed with 1% formaldehyde for 15 min in room temperature and quenched with 0.125 M glycine for 5 min in room temperature. ChIP assays was performed using a commercially available kit (ChIP-IT Express, Active Motif). Briefly, cell pellet was lysed to isolate chromatin using lysis buffer, followed by disruption with a Dounce homogenizer. LAM 621-101 cells chromatin was sheared enzymatically for 10 min at 37°C (ChIP-IT Express Enzymatic Shearing Kit, Active Motif). Immunoprecipitation was per-formed using anti-cMyc (9402, Cell Signaling) or anti-Rabbit IgG (2729, Cell Signaling) antibodies. Complexes were washed, eluted from the beads with elution buffer containing SDS buffer, and followed by RNase and proteinase K treatment. Crosslinks were reversed by incubation overnight at 65°C, and ChIP DNA was purified with a Chromatin IP DNA purification kit (Active Motif) and qPCR was performed with SYBR Green master mix on a Step One Real-Time PCR system (all Life Technologies) using the primer sets for MAP2K1, CCNB1, CDK4, RPL4, and RPL35 listed in Table S3 (Barrilleaux et al., 2013; Ciribilli and Borlak, 2017; Menssen and Hermeking, 2002).

In silico analysis of 5′ UTR structure
The Gibbs free energy and secondary structure of 5′ UTR were analyzed by the RNAfold web server (Lorenz et al., 2011): Actin (Gen-bank: NM_001101.5), BCL2 (Genbank: NM_000633.2), cMyc (Genbank: NM_002467.1), METTL3 (Genbank: NM_019852.5),

METTL14 (Genbank: NM_020961.4), ODC1 (Genbank: NM_002539.3), PPIB (Genbank: NM_000942.5), and WTAP (Genbank: NM_004906.4).

QUANTIFICATION AND STATISTICAL ANALYSIS

Data obtained from LC-MS, 2D-TLC, qPCR, immunoblot, and crystal violet staining assays are statistically analyzed using Student's t test and the graphs show mean +SD or ± SD. Statistical significance of cumulative distribution plot is determined using Tukey's HSD test. Tumor scores of *Tsc2*$^{+/-}$ mice and mRNA levels from polysome analysis are statistically analyzed using Student's t test and the error bars show mean ± SEM. Detailed methods and p value are described in figure legends and individual method sections.

Supplemental information

mTORC1 promotes cell growth

via m^{6}A-dependent mRNA degradation

Sungyun Cho, Gina Lee, Brian F. Pickering, Cholsoon Jang, Jin H. Park, Long He, Lavina Mathur, Seung-Soo Kim, Sunhee Jung, Hong-Wen Tang, Sebastien Monette, Joshua D. Rabinowitz, Norbert Perrimon, Samie R. Jaffrey, and John Blenis
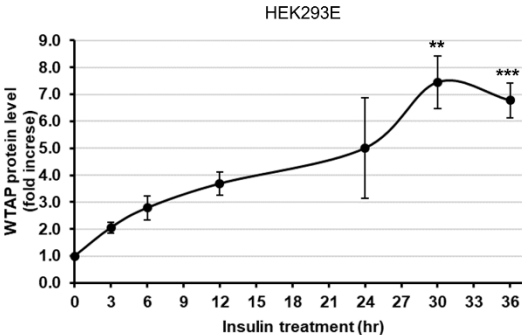
Figure S1

A
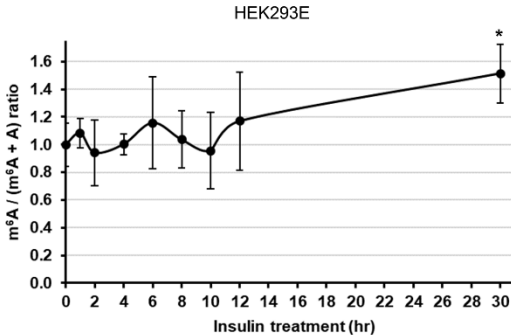
B

Figure S1. Time-course measurement of m^6A and WTAP protein levels upon insulin stimulation, Related to Figure 1.

(A) LC-MS analysis of m^6A levels in twice-purified poly(A)-RNA from HEK293E cells. Cells were treated with insulin (200 nM) for the indicated time points after overnight starvation.

(B) Immunoblot analysis of HEK293E cells treated with insulin (200 nM) for the indicated time points after overnight starvation.

$N \geq 2$. *$p < 0.05$. **$p < 0.01$. ***$p < 0.001$. Error bars show standard deviation (SD).

Figure S2

A

LAM

B

LAM

E

HEK293E

C
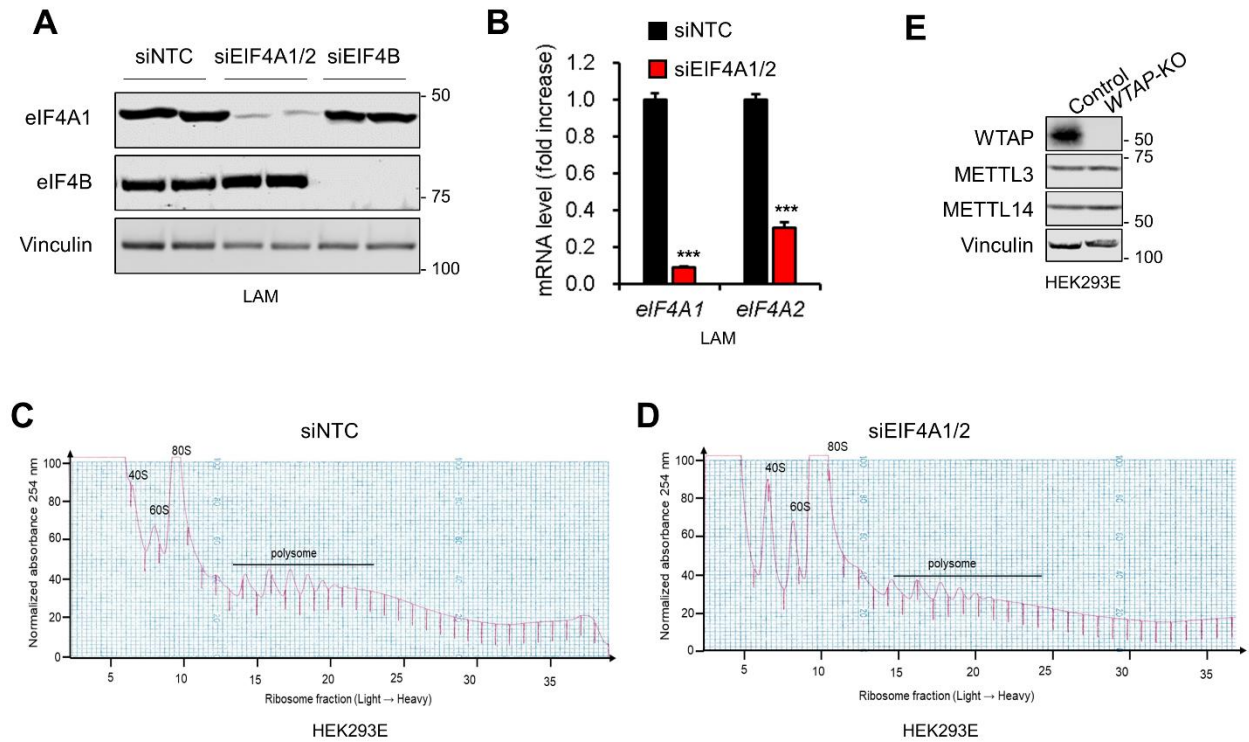

HEK293E

D

HEK293E

Figure S2. Confirmation of knockdown efficiencies, and polysome profile of *eIF4A1/2* knockdown cells, Related to Figure 3.

(A, B) Immunoblot analysis (A) and qPCR (B) of LAM 621-101 (*TSC2*^{-/-}) cells knocked down with *eIF4A1/2* or *eIF4B*.

(C, D) Sucrose-gradient analysis of polysomes from HEK293E cells knocked down with control (C) or *eIF4A* (D) siRNA.

(E) Immunoblot analysis of HEK293E cells knocked out with *WTAP.*

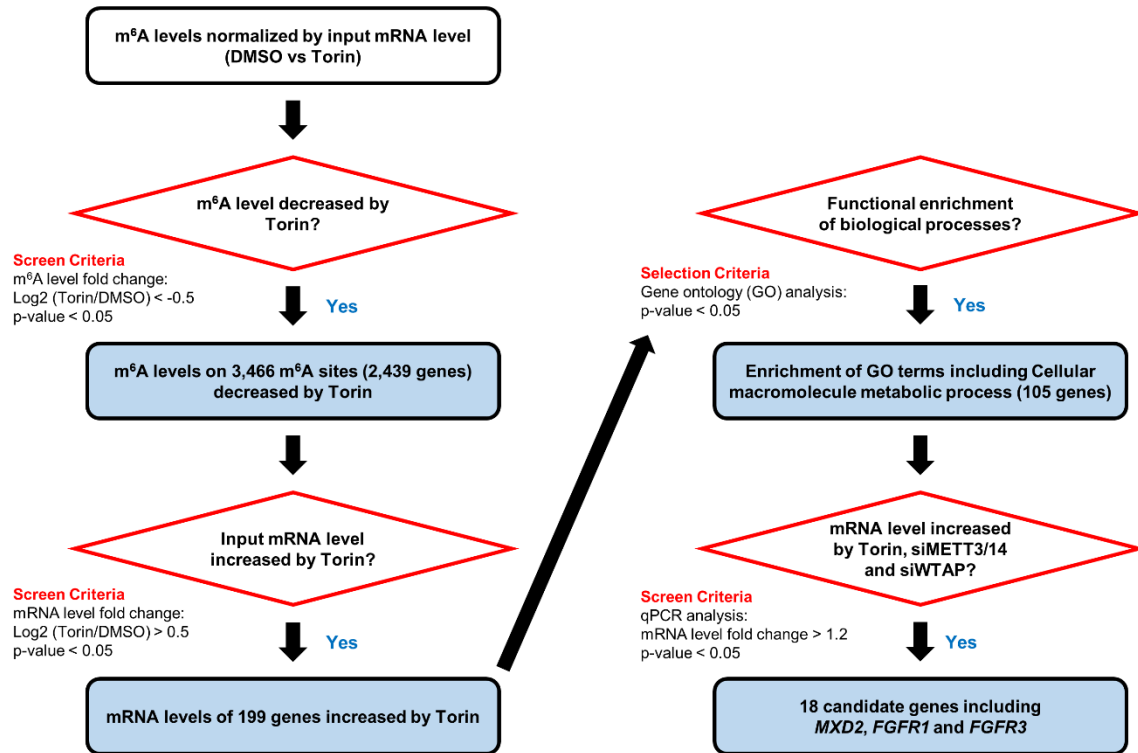N ≥ 2. ***$p < 0.001$. Error bars show standard deviation (SD).

Figure S3

Figure S3. Workflow of analysis of miCLIP candidates, Related to Figure 4.

Analysis of miCLIP and input mRNA levels in HEK293E cells (DMSO versus torin1) found 199 genes whose m^{6}A levels are decreased while mRNA levels are increased by torin1. Gene Ontology (GO) analysis revealed that over half of the genes (105 genes) are enriched in cellular macromolecule metabolic process (Supplemental Table 1). qPCR analysis of torin1-treated, and *METTL3/METTL14* or *WTAP* knocked down LAM 621-101 (*TSC2$^{-/-}$*) cells found 18 candidate genes whose mRNA levels are decreased by mTORC1 and METTL3/METTL14/WTAP (Supplemental Table 2).
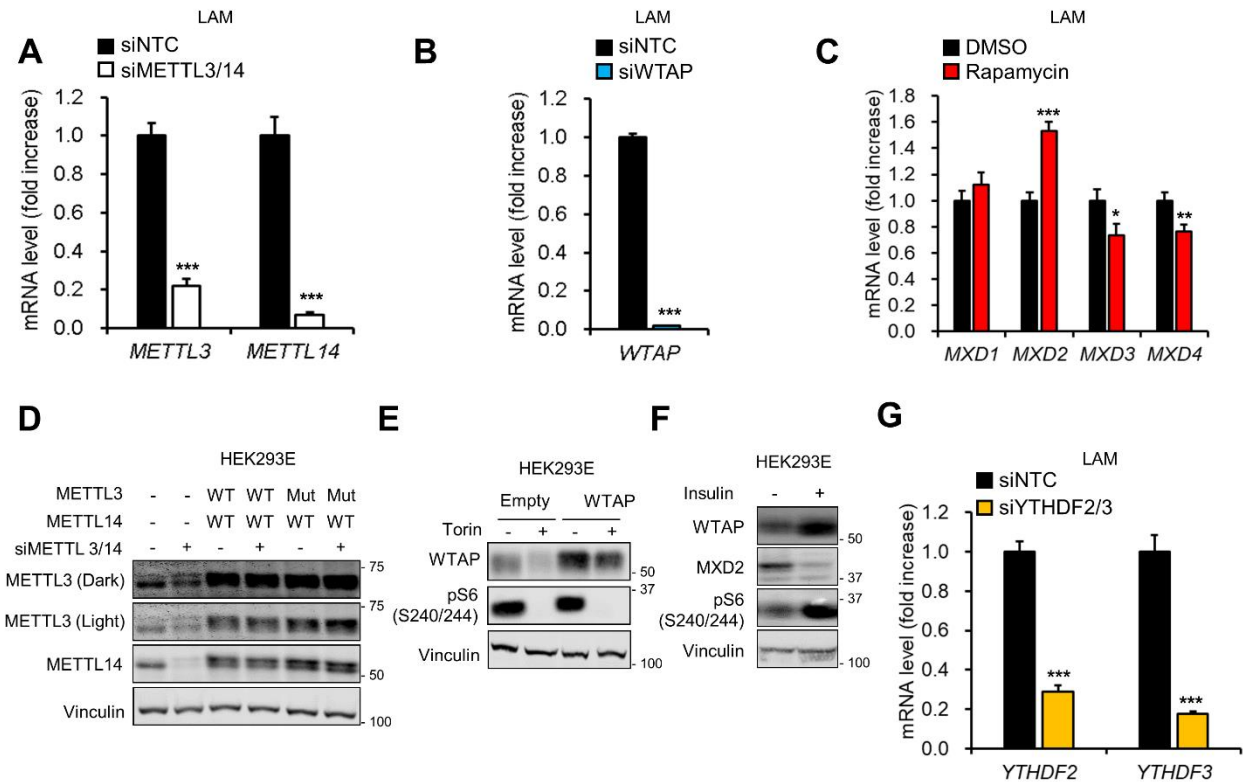
Figure S4

Figure S4. Confirmation of knockdown efficiencies, and further analysis of *MXD2* expression, Related to Figures 4 and 5.

(A, B) qPCR analysis of LAM 621-101 (*TSC2*$^{-/-}$) cells knocked down with *METTL3/METTL14* (A) or *WTAP* (B).

(C) qPCR analysis of *MXD1-4* in LAM 621-101 (*TSC2*$^{-/-}$) cells treated with rapamycin (100 nM, 24 hr).

(D) Immunoblot analysis of HEK293E cells expressing METTL14 with METTL3-WT or METTL3 catalytic dead mutant (METTL3-D395A/W398A). The cells were serum starved overnight and treated with insulin (200 nM, 30 hr).

(E) Immunoblot analysis of HEK293E cells expressing WTAP. The cells were serum starved overnight and treated with insulin (200 nM, 30 hr) with or without pretreatment of torin1 (250 nM).

(F) Immunoblot analysis of WTAP and MXD2 in HEK293E cells treated with insulin (200 nM, 30 hr) after overnight serum starvation.

(G) qPCR analysis of *YTHDF2 and YTHDF3* in LAM 621-101 (*TSC2*^{-/-}) cells knocked down with *YTHDF2* and *YTHDF3*.

N ≥ 3. *$p < 0.05$. **$p < 0.01$. ***$p < 0.001$. Error bars show standard deviation (SD).
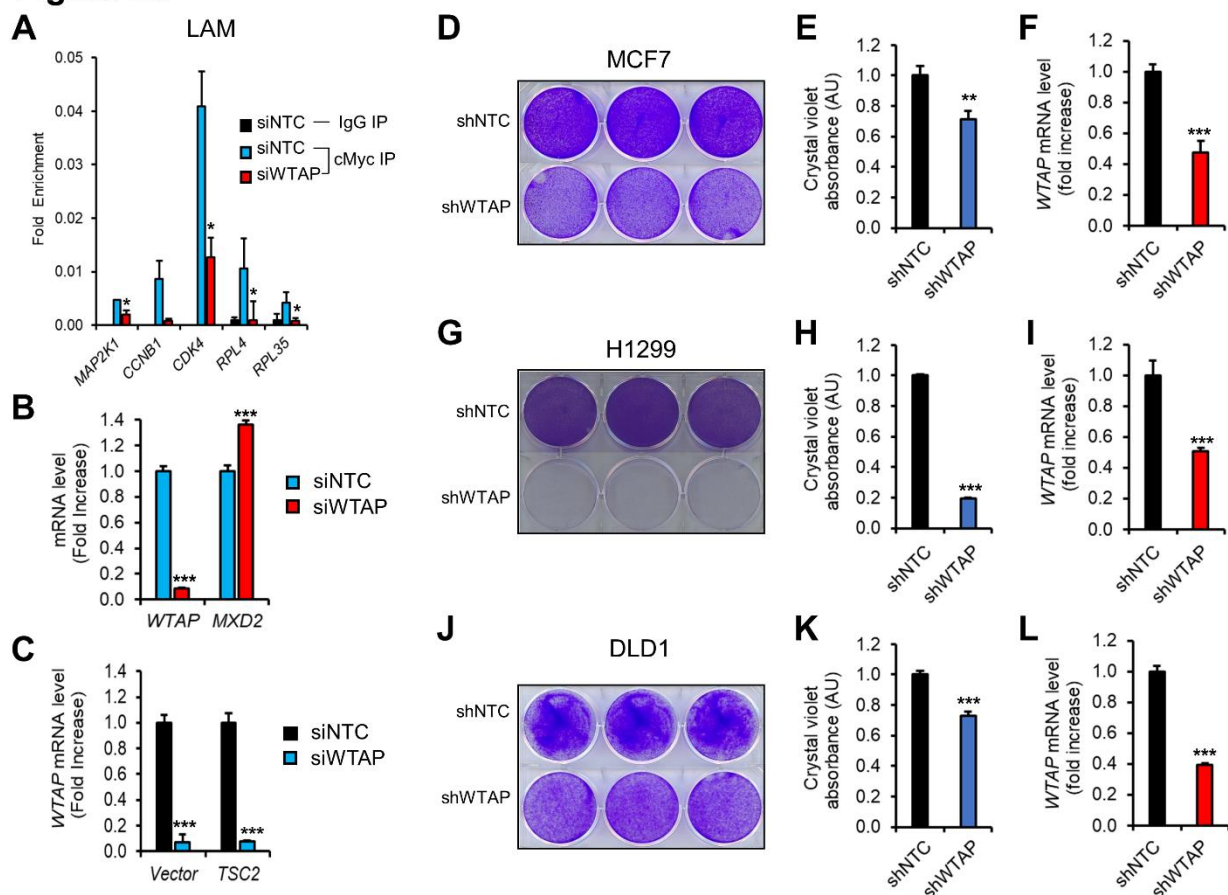
Figure S5. Further analysis of cMyc activity and growth of cancer cell panels, Related to Figure 6.

(A, B) Chromatin immunoprecipitation (ChIP)-qPCR analysis of cMyc in its target gene promoters. Immunoprecipitation was performed using IgG or anti-cMyc antibody in LAM 621-101 ($TSC2^{-/-}$) cells with knocked down with *WTAP*.

(C) qPCR analysis of LAM 621-101 ($TSC2^{-/-}$) cells expressing empty vector or *TSC2* after knockdown of *WTAP*.

(D-L) CV staining of MCF7 (D), H1299 (G), or DLD1 (J) cells after knockdown of *WTAP.* Graphs (E, H, and K) show quantified absorbance of solubilized CV dye. qPCR analysis of *WTAP* knockdown efficiency in MCF7 (F), H1299 (I), or DLD1 (L) cells.

N ≥ 3. *$p < 0.05$. **$p < 0.01$. ***$p < 0.001$. Error bars show standard deviation (SD).